



TECHNISCHE  
UNIVERSITÄT  
WIEN  
Vienna | Austria



Research Project Report  
Marshall Plan Foundation

---

# Development of Smart Bioorthogonal Chemical Tools

Conducted by

**Martin Wilkovitsch**

Institute of Applied Synthetic Chemistry, TU Wien

at the Center for Systems Biology, Massachusetts General Hospital and Harvard Medical  
School, Boston, Massachusetts, USA



June 2021 – September 2021

Supervisor TU Wien: Univ.Prof. Dipl.-Ing. Dr.techn. Johannes Fröhlich and  
Univ.Ass. Dipl.-Ing. Dr.techn. Hannes Mikula  
Supervisor MGH Boston: Jonathan Carlson, M.D. PhD

## Table of Contents

<b>1. Abstract</b> .....	<b>3</b>
<b>2. Introduction</b> .....	<b>4</b>
2.1 Bioorthogonal Chemistry .....	4
2.2 Tetrazine Ligation .....	6
2.3 Click-Only .....	7
2.4 Click-to-Release .....	7
2.5 C <sub>2</sub> TCO .....	9
2.6 Multiplexed Profiling in Live Cells .....	10
<b>3. Results</b> .....	<b>11</b>
3.1 Bioorthogonal Cooperativity Accelerates Scission .....	11
3.2 Cycling in Live Cells .....	13
3.3 Profiling the Differentiation of Living Bone Marrow .....	15
<b>4. Discussion</b> .....	<b>17</b>
<b>5. Experimental Methods</b> .....	<b>19</b>
5.1 Synthesis and Characterization .....	19
5.2 Probe Activation .....	24
5.3 Click and Scission Kinetics .....	24

## 1. Abstract

In 2020, estimated 20 million people were diagnosed with cancer occupying one of the world's leading causes of death. Over the past decades, many efforts have been made to design new molecular tools for reliable diagnostic analysis of malignant diseases. After all, effective alternatives for the accurate detection of malicious tissue are currently of desperate need more than ever and medicinal strategies to specifically control disease processes still remain at an early stage.

The development of chemical reactions that can safely and selectively be carried out in living systems has enabled the concept of *in vivo* chemistry. Biocompatible chemistries have become powerful tools providing researchers with highly selective methods to achieve and control chemical events in complex biological environments. Since its introduction, bioorthogonal chemistry has held great promise to address these challenging demands by enabling scientists to perform chemical transformations in living systems and thereby to study biomolecules within their native habitat while not interfering with the biological functions therein. Among all bioorthogonal chemistries developed, none came close to the performance characteristics of the reaction between *trans*-cyclooctenes (TCOs) and 1,2,4,5-tetrazines (Tz), also referred to as "tetrazine ligation". Due to the high selectivity of the reaction partners, excellent biocompatibility and most importantly its exceptional reaction kinetics, the tetrazine ligation has become an indispensable tool for *in vitro* and most notably *in vivo* applications of bioorthogonal chemistry. Besides the solely formation of new covalent linkages, the concept of bond-cleavage reactions using Tz/TCO chemistry ('click-to-release') has further expanded the repertoire of bioorthogonal methods to precisely deliver and activate drugs at the site of disease. Nevertheless, especially for the release of (bio)active cargos, complex chemical, biological, and pharmacokinetic factors still remain as hurdles to the design of new targeted therapeutics. However, existing bioorthogonal tools have not reached the level of performance required for effective and safe *in vivo* application, mainly due to insufficient reaction kinetics (i.e. speed of the chemistry at low, non-toxic concentrations) and limited efficiency (i.e. overall outcome of the reaction). To selectively and reliably compete with biological processes, there is a need for ultrafast bioorthogonal cleavage reactions that can be performed at low concentrations (sub-nM to  $\mu\text{M}$ ).

The objective of this research project was to bridge the divide between highest reactivity and outstanding efficiency of the release event of currently available bioorthogonal tags to be applied in diagnostics. Based on the scaffold of the cleavable  $C_2$ -symmetric TCO-linker ( $C_2\text{TCO}$ ) developed in our we combined its beneficial release properties and excellent stability for the application in ultra-fast cycling for multiplexed fluorescence imaging in live cells.

## 2. Introduction

### 2.1 Bioorthogonal Chemistry

Bioorthogonal chemistry refers to chemical reactions capable of forming covalent linkages in the highly complex environment of living systems not interfering with native biological processes therein. Typically, two functional groups react selectively, with each other that are absent in the natural settings enabling the study of biomolecules within their native habitat.<sup>1-4</sup>

This biochemical inertness to the vast number of functionalities present together with sufficient metabolic stability for a prolonged timeframe are key requirements for both, bioorthogonal reaction partners and their products.<sup>3,5</sup> Moreover, highest degree of selectivity to avoid any interaction with cellular functions as well as excellent biocompatibility with the native environment in living organisms are mandatory. Reaction kinetics of bioorthogonal ligations must be exceptionally fast to reach reasonable reaction times at the very low (sub-) micromolar concentrations in native systems. Furthermore, a bioorthogonal reaction must proceed in aqueous media, at physiological pH, and at body temperature causing no drop in reactivity (Figure 1).<sup>6-8</sup>

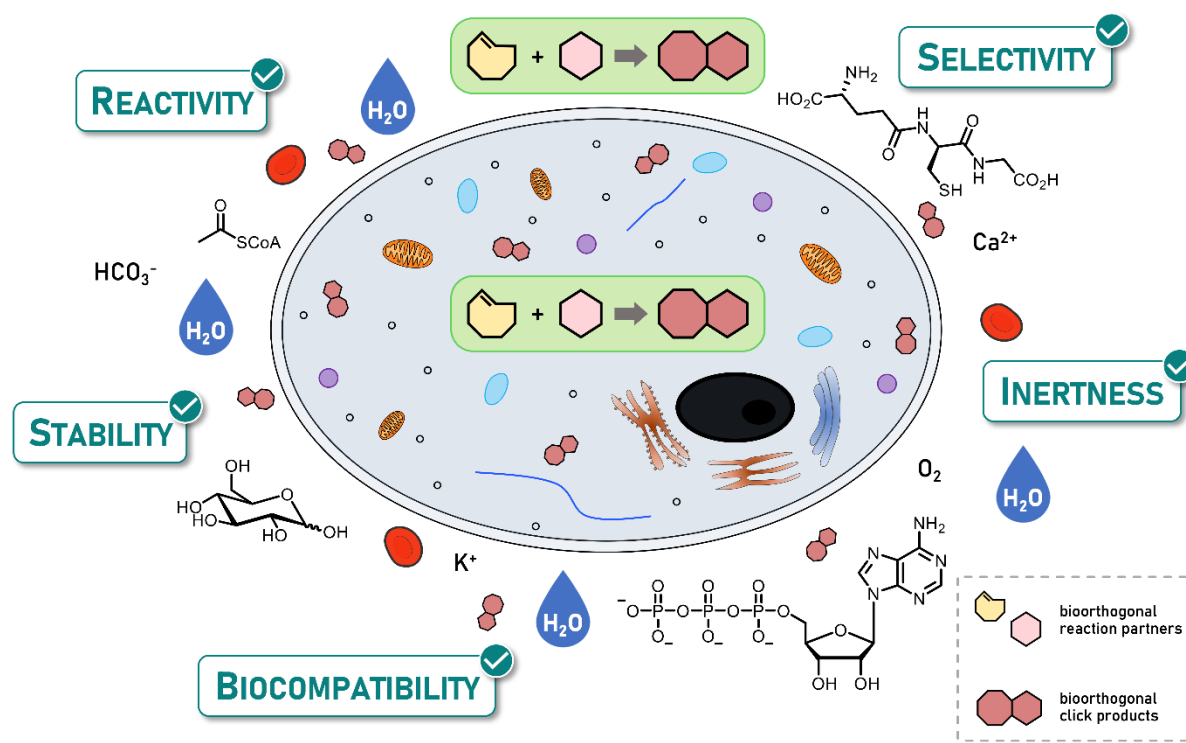


**Figure 1.** Bioorthogonal reaction partners are capable of reacting within the complex environment of living systems, even inside of mammalian cells.

This concept with its very challenging demands was coined by the pioneering work of Eliana Saxon and Carolyn Bertozzi who have revolutionized the fields of chemical biology and bioorganic chemistry in the early 2000s.<sup>9</sup> The introduction of the Staudinger ligation, on the basis of the Staudinger reaction between triarylphosphines and azides represented the first reaction with completely abiotic functional groups. Although this bioorthogonal reaction has been successfully applied in mice and living cells, it remains to be no longer widely used due

to poor reaction kinetics and the phosphine reagent very prone to undergo oxidation *in vivo* (Figure 2, top).<sup>7, 9, 10</sup>

Over the years, especially cycloadditions have proven to be highly useful for bioorthogonal applications.<sup>11</sup> The copper(I)-catalyzed azide-alkyne [3+2] dipolar cycloaddition (CuAAC) developed independently by the groups of Barry K. Sharpless<sup>12, 13</sup> and Morten Meldal<sup>14</sup> created a breakthrough in click chemistry, but due to the cytotoxic nature of copper, CuAAC was inapplicable in living organisms thus failing to meet the stringent requirements for bioorthogonality (Figure 2, middle). The need for a (copper-) catalyst was eliminated by using strained alkynes leading to the strain-promoted azide-alkyne cycloaddition (SPAAC) introduced also by the Bertozzi group in 2004.<sup>15, 16</sup> Despite reaction kinetics were slower compared to the CuAAC, a more than 60-fold enhancement in reactivity could be achieved for first-generation SPAAC-reagents in contrast to the Staudinger ligation. In combination with its incredible bioorthogonality and further improved rate constants<sup>17</sup>, the SPAAC allowed imaging in zebra-fish<sup>18</sup>, mice and live-cells<sup>19</sup> and is still commonly used in various research applications to the present day. The reaction kinetics of SPAAC, however, remains to be too slow for monitoring dynamic biological processes *in vivo* (Figure 2, bottom).

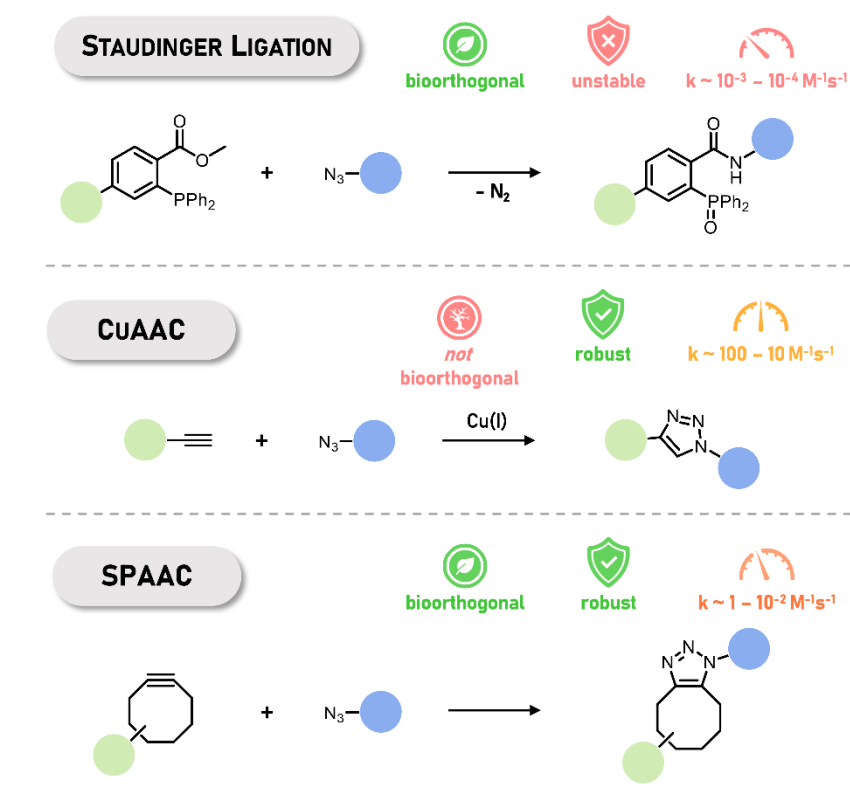


**Figure 2.** Chemical reactions applied in chemical biology and their characteristics (bioorthogonality, stability, second-order rate constants).

In the meantime, several other bioorthogonal cycloaddition reactions have been developed including nitrones,<sup>20</sup> norbornenes,<sup>21</sup> oxanorbornadienes,<sup>22</sup> tetrazoles (“photoclick chemistry”)<sup>23, 24</sup> or the quadricyclane ligation<sup>25</sup> but most of these were limited to *in vitro* applications mainly due to their unfavorable reaction conditions or -characteristics.

## 2.2 Tetrazine Ligation

So far, none of the bioorthogonal transformations established came close to the chemical performance of the reaction between strained *trans*-cyclooctenes (TCOs) and 1,2,4,5-tetrazines (Tz) also referred to as the ‘tetrazine ligation’. Independently introduced by the groups of Joseph M. Fox<sup>26</sup> and Ralph Weissleder<sup>27</sup> in 2008, the tetrazine ligation proceeds in highest yields, exhibits outstanding biocompatibility and reaches unprecedented fast reaction constants of millions  $M^{-1}s^{-1}$ , most notably in aqueous solutions. Furthermore, with rather straightforward synthesis of the reaction partners most of them proving to be highly stable in biological media, this ligation meets all requirements making it the most optimal bioorthogonal reaction to date.<sup>28, 29</sup>

The mechanism behind consists of an inverse electron-demand Diels-Alder (IEDDA) [4+2] cycloaddition between the diene (Tz) and the strained dienophile (TCO) in the first step (‘Click’). The highly strained bicyclic adduct undergoes a retro Diels-Alder reaction causing the elimination of inert nitrogen gas and the initial 4,5-dihydropyridazine (4,5-DHP) is formed. Subsequent isomerization leads to the 1,4-dihydropyridazine (1,4-DHP) and upon oxidation the fully aromatic final click product is obtained (Figure 3).<sup>30, 31</sup> The tetrazine ligation has set a new milestone in the world of bioorthogonal concepts<sup>31</sup> making it suitable in respect of biological time scales equipped with an increased signal-to-noise ratio. Thus, the applications for this bioorthogonal ligation widely range from many kinds of biomedical research<sup>32, 33</sup> to materials science<sup>34, 35</sup>.

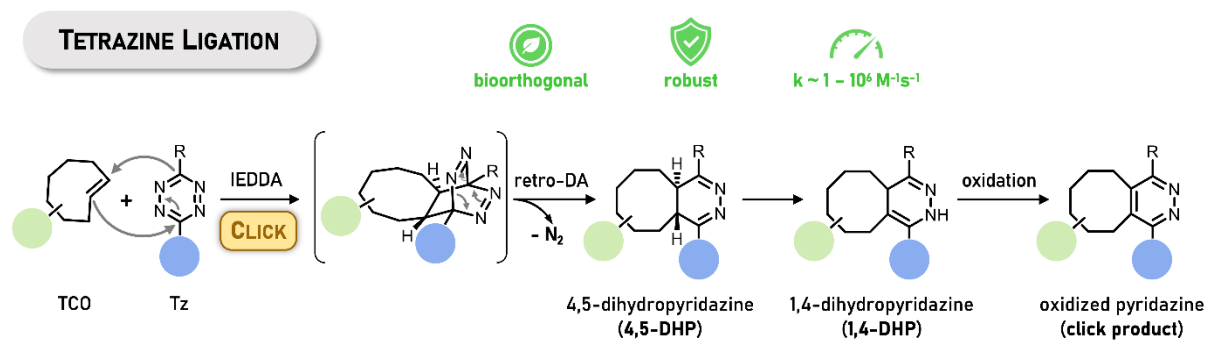


Figure 3. Mechanism of the tetrazine ligation with its characteristics (bioorthogonality, stability, second-order rate constant).

Compared to the rich methodology of organic reaction mechanisms, only two types – addition and elimination reactions – have been explored for general bioorthogonal chemistry. The tetrazine ligation provides both, spatiotemporal control of molecular assembly (‘Click-only’) and even disassembly (‘Click-to-release’) representing a versatilely applicable toolkit.

## 2.3 Click-Only

The tetrazine ligation relies on the bioorthogonal addition reaction of TCO and Tz for the merely purpose of connecting (bio-)molecules with each other by the formation of new covalent linkages (Figure 4). With providing the opportunity for extensive chemical optimization and substantial tuning of its click-performance, the tetrazine ligation centralizes aspects wherever fast and efficient connectivity is of desperate need. As a consequence, this bioorthogonal cycloaddition not only set a landmark in chemical biology but also left remarkable footprints in the field of nuclear medicine.<sup>36, 37</sup>

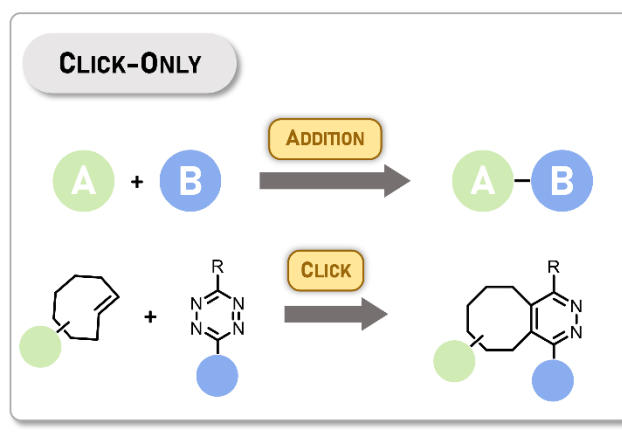


Figure 4. Click-only approach of the bioorthogonal tetrazine ligation.

## 2.4 Click-to-Release

In addition to click-only applications, the concept of bond-cleavage reactions using Tz/TCO chemistry has further expanded the repertoire of chemical methods to diagnostic and therapeutic applications in chemical biology. Inspired by the selective cleavage on basis of the Staudinger ligation, Robillard and co-workers designed an efficient bioorthogonal elimination system by modifying the existing tetrazine ligation consisting of an allylic, carbamate-bearing TCO (release-TCO, rTCO) and a tetrazine. The initial click step remains the same as in the bioorthogonal addition reaction giving the corresponding 4,5-dihydropyridazine (4,5-DHP). Via the click-to-release methodology this intermediate subsequently undergoes 1,4-elimination by deprotonation, releasing  $\text{CO}_2$  and the leaving group as a free amine (Figure 5).<sup>38</sup>

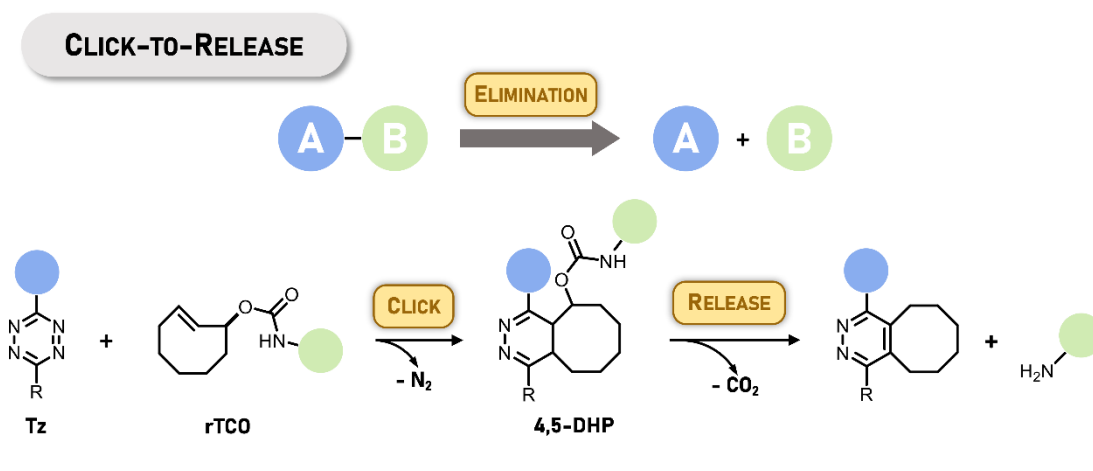
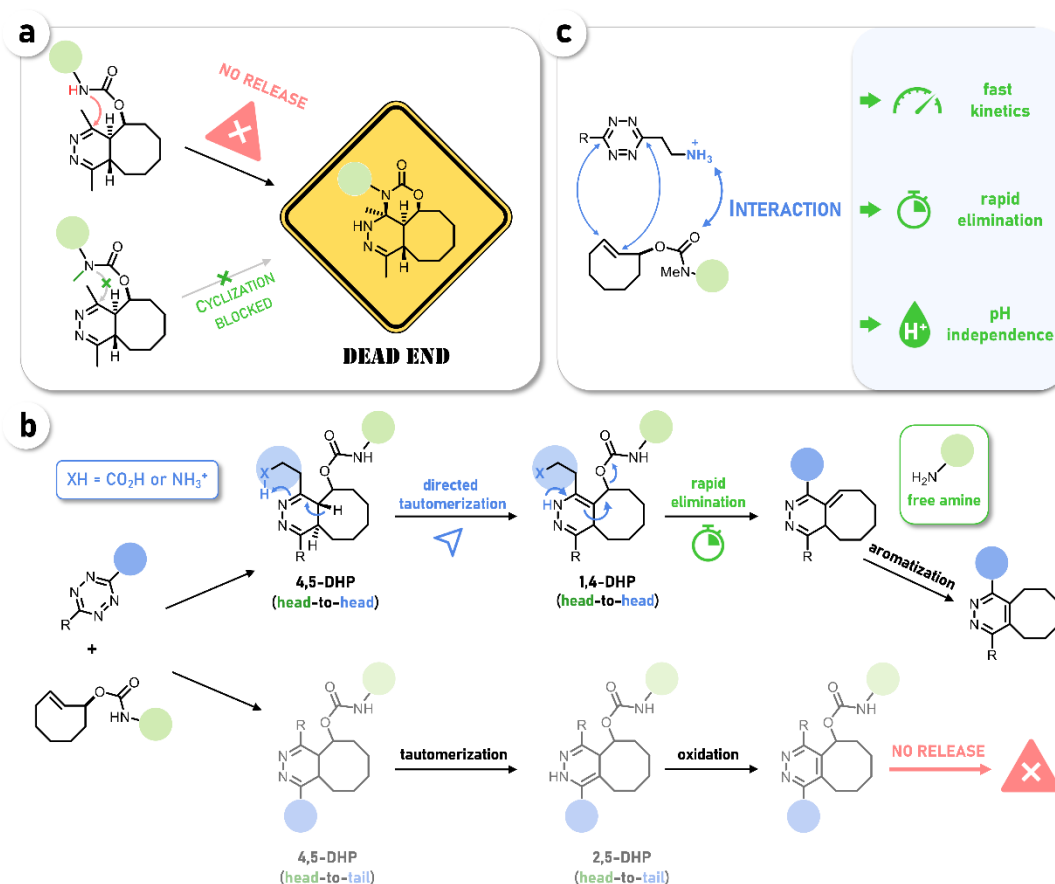


Figure 5. Click-to release approach of the bioorthogonal tetrazine ligation.

But this methodology was limited to incomplete and/or slow release in its first appearance due to unknown tautomerization and isomerization events proceeding after ligation. The delicate pH sensitivity and the critical role of those post-click processes was uncovered by Carlson *et al.* who shed light on the detailed mechanism behind the Tz-triggered pyridazine elimination. First they identified intramolecular cyclization as the main reason for the poor release performance of rTCO with bis-alkyl-tetrazines resulting in the formation of a dead end isomer not capable of undergoing release.<sup>39</sup> This undesired pathway could be circumvented by blocking the nucleophilic addition of the carbamate with N-methyl substitution (Figure 6a). Furthermore, also the click orientation between Tz and rTCO has been shown to strongly affect the release event after ligation as it directs the tautomerization towards effective liberation of the free amine. Thereby, the use of tetrazines bearing directing groups such as carboxylic acids or ammonium substituents have proven to promote the elimination performance via intramolecular proton-donation in the initial click product (4,5-DHP).<sup>39-41</sup> For this desired outcome to happen, the directing group on the Tz needs to be positioned categorically next to the allylic-releasing end of the rTCO ('head-to-head'). On the other hand, the head-to-tail click orientation leads to the corresponding 2,5-dihydropyridazine (2,5-DHP) from which the elimination of the cargo is disabled (Figure 6b). In this context, the group of van Kasteren provided great insight by revealing that if ammonium-ethyl residues on the tetrazine are used, the head-to-head case is even the favored click orientation towards release-TCO due to



**Figure 6.** (a) Intermolecular cyclization forming a dead-end-product can be prevented by *N*-methylation. (b) Accepted mechanism of post-click tautomerization with Tz bearing directing groups enabling fast and efficient release. (c) Ammonium residues on Tz interact with the carbamate moiety of the TCO to reach high click AND release rates, and show pH-independence in aqueous media.

interaction of the cationic ammonium functionality with the polar carbamate group.<sup>41</sup> These findings not only led to a significant increase in click- and elimination kinetics but also to a new generation of pH independent tetrazines especially important in the release step (Figure 6c). However, by the combination of high reactivity and selectivity with the opportunity for releasing incorporated cargos very efficiently, bioorthogonal bond-cleavage approaches are nowadays used in widespread biomedical research areas. *In vitro* applications include uncaging of fluorogenic compounds<sup>40, 41</sup> and enzyme substrates<sup>42</sup> as well as cell-specific proteome labeling<sup>43</sup>. More remarkably, this concept has emerged mainly in the field of targeted drug delivery with *in vivo* applications like cleavage of antibody-drug-conjugates (ADCs),<sup>44, 45</sup> prodrugs,<sup>46</sup> nanoparticles,<sup>47</sup> and proteins<sup>48, 49</sup> by the administration of the Tz as activator.

## 2.5 C<sub>2</sub>TCO

As discussed, improvements in the liberation of installed cargos on TCOs modified in allylic position could be achieved by the use of tetrazines bearing aliphatic substituents with carboxy- or amino-functionalities, acting as proton donors effectively directing the tautomerization of the initial click product accelerating the elimination step (*vide supra*). But in the early years

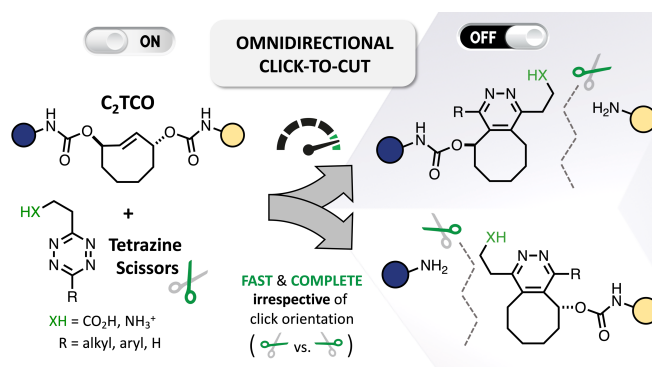


**Figure 7.** C<sub>2</sub>-symmetric TCO enables fast and complete bioorthogonal disassembly irrespective of click orientation.

only less reactive bis-alkyl-tetrazines could be used to reach complete cleavage, while highly reactive aryl- and H-Tz gave only very limited release yields. In contrast to targeted activation and similar turn-ON approaches for which a relatively broad range of release yields may generate discernible signal and/or relevant downstream activity the combination of fast AND complete cleavage is essential for turn-OFF strategies to reach minimal function within biological time scales. Effective cleavage of the rTCO scaffold is challenging due to critical tautomerization and isomerization events occurring after ligation and heavily relies on the click orientation between the Tz and the TCO. This issue was tackled by us by the design and synthesis of a C<sub>2</sub>-symmetric *trans*-cyclooctene linker (C<sub>2</sub>TCO)<sup>50</sup>. Due to the two allylic release positions overall cleavage is independent from the click orientation with tetrazines (Figure 7). Applying C<sub>2</sub>TCO in combination with a new generation of mono- and aryl-substituted Tz bearing carboxylic acid- or ammonium-functional groups enabled us to achieve both, fast (instant) and complete (>99%) cleavage, thus fulfilling the stringent requirements for bioorthogonal turn-OFF. By incorporation of C<sub>2</sub>TCO into an antibody-dye conjugate, fast extracellular bioorthogonal cleavage within minutes was accomplished. In addition, efficient intracellular disassembly was demonstrated via omnidirectional tetrazine-triggered cleavage of an ibrutinib-C<sub>2</sub>TCO-dye conjugate. These results indicate the potential of C<sub>2</sub>TCO to enable advanced methods for bioorthogonal turn-OFF applications even *in vivo*.

## 2.6 Multiplexed Profiling in Live Cells

Temporal processes are often studied in living cells and organisms by introducing fluorescent proteins coupled to a promoter<sup>52</sup>, protein<sup>53</sup>, or biological compartment<sup>54</sup> of interest, making otherwise invisible physiologic events observable by fluorescence microscopy. This strategy has been intensely successful in cell biology<sup>55</sup>. However, the approach is not without shortcomings, including: i) the time required for creation and validation of cell lines; ii) the limited number of concurrent targets that can be visualized; and iii) the practical impossibility of using fluoroprotein labeling to analyze intact ensembles of primary cells, especially in complex contexts like development, differentiation, or immune function. Optimized monoclonal antibodies make immuno-fluorescence techniques a feasible alternative to study genetically unmodified cells both *in vitro*<sup>56</sup> and *in vivo*<sup>57,58</sup>, but only for a handful (i.e. 1-4) of simultaneous targets. In aggregate, these liabilities sharply restrict the dimensionality of our view into living systems.

An array of analytical technologies, such as cellularly-resolved sequencing<sup>59-62</sup>, highly multiplexed immunostaining<sup>63-66</sup>, mass/imaging cytometry<sup>67-70</sup>, and synergistic combinations thereof<sup>71,72</sup>, can now achieve detailed snapshots of biomarker abundance, producing fine-grained but static profiles. Nevertheless, the techniques are thus far incompatible with making measurements in live cells, due to inherently lethal physicochemical processing during the analytical workflow or dissociative single-cell detection, as in flow cytometry<sup>73</sup>. Of the above tools, only the methods that rely on iterative immunostaining are potentially non-destructive, as the key step of antibody-antigen recognition is intrinsically biocompatible. The competing priorities, however, of fast/complete cycling (for efficient multiplexing with adequate signal to noise) and gentleness/non-toxicity (leaving cells both alive and unperturbed) require chemical conditions that have remained many orders of magnitude apart. As a result, highly multiplexed temporospatial profiling of living cells has been virtually impossible.

Lacking such methods, certain biological processes have remained challenging to investigate, for example: i) the role of intercellular communication in differentiation<sup>56,74</sup> or immunotherapy<sup>75,76</sup>, ii) functional exploration of novel cellular phenotypes, particularly in the space of immunology<sup>77-79</sup>; iii) tracing of cellular lineages, e.g. in hematopoietic development<sup>80</sup>. In each case, experiments can provide inferential evidence: patterns of ligand-receptor gene expression and spatial colocalization in fixed tissue samples allow deduction of likely cellular interactions<sup>81</sup>; barcoding and functional readouts of knock-in/out experiments can identify cellular fate and physiologic roles<sup>82</sup>. Methods that can instead directly observe these events offer the possibility of interrogating biological interactions, developmental transformations, and the downstream responses. Further development of such dynamic model systems has thus far been hindered by our inability to efficiently visualize both biomolecular complexity and (multi)cellular dynamics in real time.

Within this project we envisioned that new bioorthogonal chemistries could achieve the capabilities needed for longitudinal multiplexed profiling in live cells (Figure 8). Therefore, our goal was the development and application of the scission-accelerated fluorophore exchange

(SAFE) method, which leverages cooperative bioorthogonal mechanisms to first quench and then completely remove fluorescent signal from antibody-labeled cells. With a scaffold built around the cleavable C<sub>2</sub>-symmetric *trans*-cyclooctene (C<sub>2</sub>TCO)<sup>50</sup>, SAFE exploits non-covalent quencher-fluorophore interactions to accelerate already rapid tetrazine (Tz)-TCO click reactions, reaching >99% scission in seconds. Critically, this makes bioorthogonal cycling feasible at nontoxic nanomolar concentrations which was not possible with prior methods<sup>83</sup>, all while achieving the high signal to background needed for serial profiling. We first quantified the accelerated chemical kinetics in analytical fluorescence assays and verified the scission performance in the biological context by time-resolved imaging. We then proceeded to validate the accuracy and nontoxicity of 14 color imaging of living mouse peripheral blood mononuclear cells (PBMCs) and visualized myeloid subsets in multicolor staining of living murine bone marrow. Last, we demonstrate the ability of serial bioorthogonal cycling to track the differentiation of immortalized hematopoietic progenitor cells into neutrophils in longitudinal profiling of the same cells over 6 days.

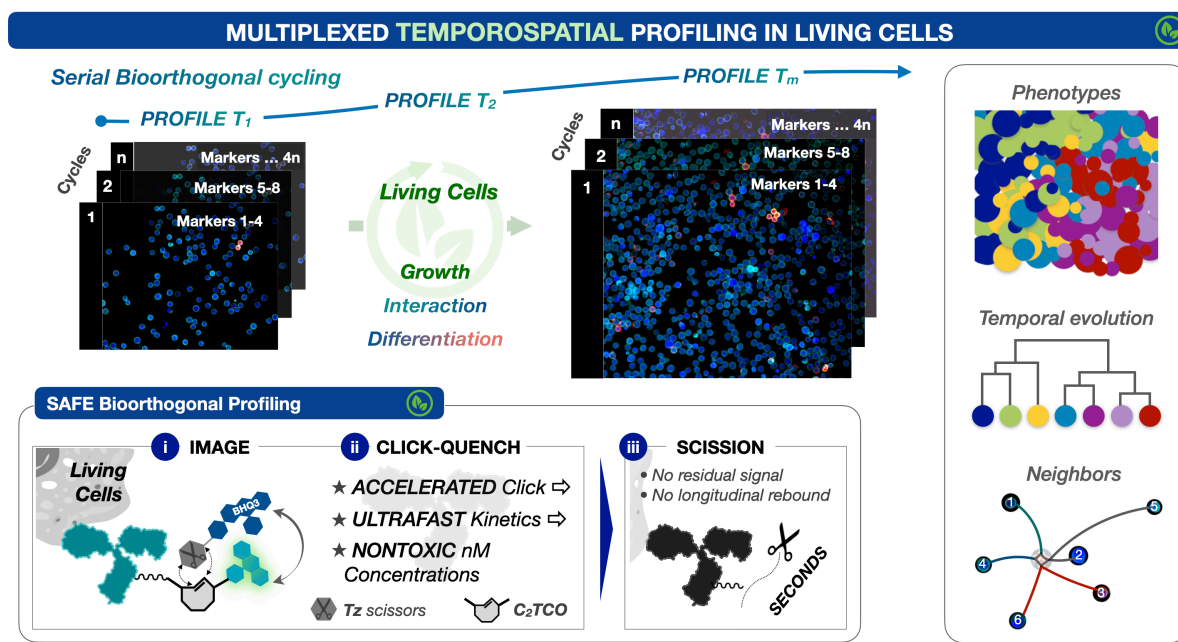


**Figure 8.** Serial bioorthogonal cycling can reveal complex cellular dynamics in living cells, enabling phenotypic characterization and longitudinal tracking of temporal evolution and/or neighbor-neighbor interactions. *Inset:* the design of scission-accelerated fluorophore exchange (SAFE) combines a hyperaccelerated click-quenching reaction with rapid fluorophore scission to gently, efficiently, and irreversibly erase fluorophores from the surface of immunostained living cells in seconds.

## 3. Results

### 3.1 Bioorthogonal Cooperativity Accelerates Scission

For all but the most reactive molecules, chemical processes that reach completion in the timeframe of seconds to minutes require concentrations in the high micromolar to millimolar range. While this is no obstacle for *in vitro* organic synthesis, it poses challenges for bioorthogonal methods: i) these same concentration ranges correspond to the level at which many organic compounds become nonspecifically cytotoxic, barring use in living cells; ii) reagents with this highest degree of reactivity are typically metastable and/or vulnerable to

rapid degradation, limiting their performance in the biological environment<sup>84</sup>. To circumvent these issues, the design of SAFE exploits a cooperative interaction between the fluorescence quencher BHQ3 and Alexa Fluor dyes for rapid on/off scission of fluorophore-C<sub>2</sub>TCO-labeled antibodies (Figure 9a) at low, nontoxic reagent concentrations. Importantly, the BHQ3-dye interaction is expected to accelerate the Tz-TCO click reaction; in this initial stage, ligation yields immediate quenching (>95%) of the dye fluorescence<sup>83</sup>. In turn, quantitative scission is driven by a functionalized tetrazine equipped with an intramolecular proton donor (NH<sub>3</sub><sup>+</sup> at physiologic pH) that serves to accelerate tautomerization, functioning as a ‘Tz-scissors’<sup>39,41,50</sup>. This click-to-cut scission reaction then releases the quenched fluorophores from antibodies, removing residual signal: i) optimizing signal to background, and ii) eliminating the downstream risk of rebounding signal from the quenched dye.

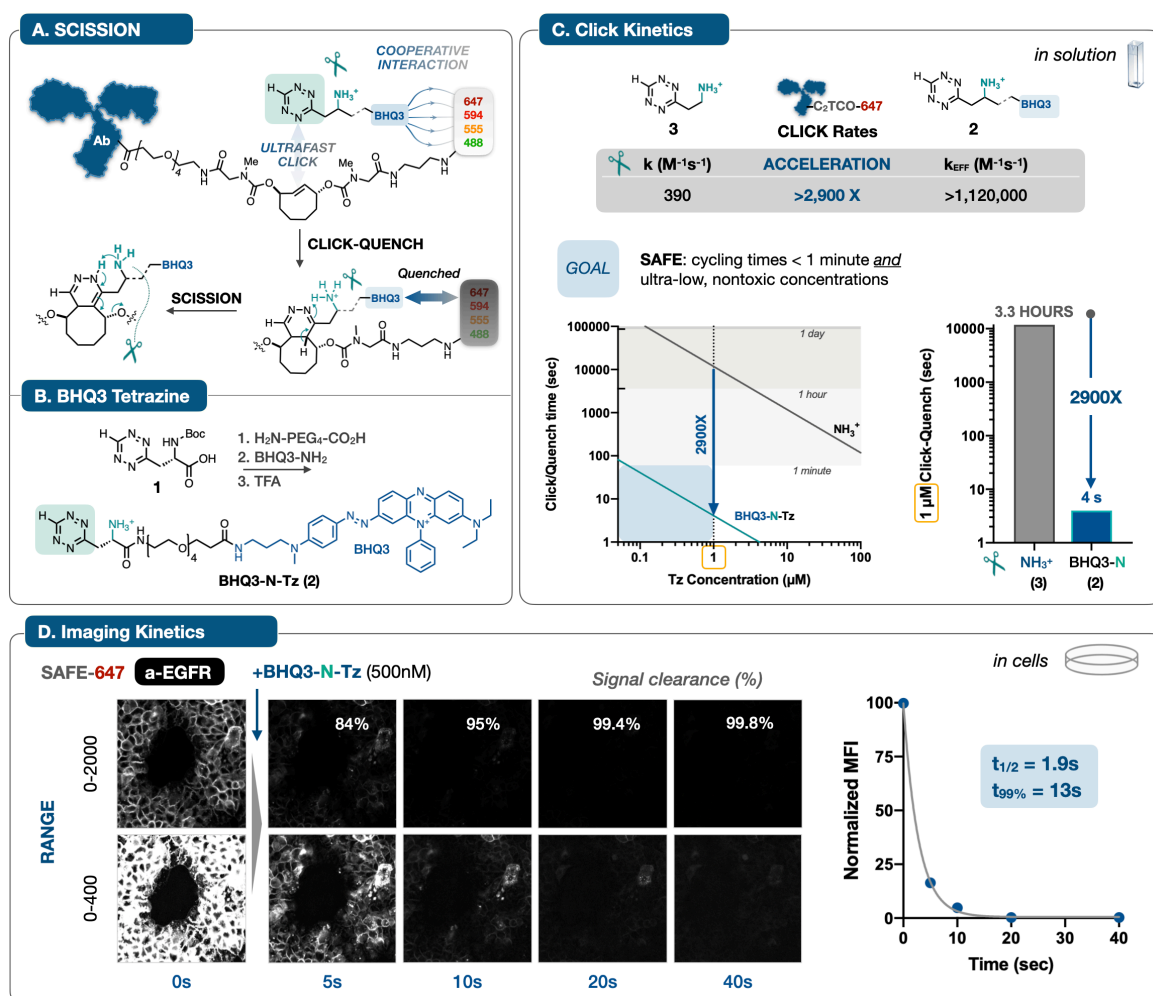


**Figure 9.** (a) Antibodies labeled with C<sub>2</sub>TCO-linked dyes are rendered non-fluorescent in a concerted two step sequence: noncovalent interactions between BHQ3 and the fluorophore can accelerate the Tz/TCO click reaction<sup>83</sup>, leading to immediate quenching upon ligation; in turn, the functionalized ‘Tz-scissors’ drives instantaneous tautomerization and scission of the dye. (b) Starting from the Boc-protected Tz, a hydrophilic PEG linker and BHQ3 are conjugated and then deprotected to yield BHQ3-N-Tz (2). (c) Quantification of reaction kinetics for the click reaction of 2 with an AF647-C<sub>2</sub>TCO-labeled antibody in solution revealed an effective rate constant of >10<sup>6</sup>, a marked 2,900-fold acceleration relative to the parent aminoethyl-functionalized Tz (3)<sup>50</sup>. This acceleration shifts the concentration/time relationship into the needed range for efficient cycling at ≤ 1 μM reagent concentrations. (d) To validate the accelerated kinetics in the cellular context, we collected time lapse images of A431 cells stained with a SAFE647-anti-EGFR antibody and then treated with BHQ3-N-Tz (2). Background-subtracted images rendered at two window levels capture the rapid ( $t_{1/2} = 1.9$  s) and quantitative clearance of the fluorophore signal, reaching 99.8% removal within 40 seconds, concordant with the in vitro assay measurements.

We therefore synthesized N-Boc-protected tetrazine and extended it with a PEG<sub>4</sub> amino acid linker, followed by coupling with BHQ3 amine and deprotection (Figure 9b). The reaction of BHQ3-N-Tz (**2**) and an AF647-C<sub>2</sub>TCO (SAFE647) labeled antibody was followed by monitoring fluorescence intensity vs time. At an optimized concentration of **2**, the reaction process could be kinetically segregated into its two component phases, resolving the quenching of the click ligation from the subsequent scission reaction. Nonlinear fitting of the biphasic fluorescence timecourse yielded a rate constant of  $0.133 \pm 0.005 \text{ s}^{-1}$  ( $t_{1/2} = 5.2$  seconds) for the scission of the C<sub>2</sub>TCO linker. For the click ligation itself, we measured an effective second order rate constant  $\geq 1.12 \times 10^6 \text{ M}^{-1}\text{s}^{-1}$ , more than 2900-fold faster than the reaction of the parent Tz (**3**) with C<sub>2</sub>TCO<sup>50</sup>. C<sub>2</sub>TCO itself is stable (>97% intact at  $t = 48\text{h}$  in full cell growth media) and not very reactive until accelerated by the ‘cooperative’ SAFE effect, resulting in stable click reagents, but also very fast kinetics.

This shifts the kinetic regime from hours to seconds: a benchmark concentration of  $1 \mu\text{M}$  is predicted to reach complete (>99%) reaction in 4 seconds, while nanomolar concentrations are sufficient for complete click-quench reactions in less than a minute, matching the design objectives (Figure 9c). To validate the solution kinetics in a biological context, we stained fixed A431 cells with a SAFE647-labeled anti-EGFR antibody and collected serial images before and after the addition of BHQ3-N-Tz (500 nM, Figure 9d). The quenching-cleavage reaction on the surface of the cells was both rapid ( $t_{1/2} = 1.9 \text{ s}$ ) and complete, with a 99.8% reduction in signal intensity after 40 seconds, (~8 scission half-lives). This kinetics integrate both steps of signal removal at the extracellular surface, confirming the magnitude of the acceleration and the high dynamic range of signal elimination, critical to preventing background accumulation across multicycle staining.

### 3.2 Cycling in Live Cells

We performed an initial short term cycling experiment on live A549 cells stained with Hoechst and a SAFE647-conjugated anti-N-Cadherin antibody. The N-Cadherin signal was efficiently eliminated with BHQ3-N-Tz ( $1 \mu\text{M}$ , 1 minute, Figure 10a). A fraction of cells visually confirmed their live status by undergoing mitosis during the imaging process: in the example shown (Figure 10a, inset) a cell is captured in metaphase before quenching and in early anaphase after quenching, 17 minutes of elapsed time later. For a longer-term assessment, we expanded the A549 experiments into serial imaging to test scission performance and screen for cytotoxicity. Cells were stained with a SAFE647-conjugated anti-EGFR antibody, quenched/cleaved with BHQ3-N-Tz, and then returned to routine culture conditions at  $37 \text{ }^\circ\text{C}$ , with images of the same cellular area collected at each stage. After 24 hours, the cells were then re-imaged with live and dead cell staining dyes (live: calcein AM, dead: sytox red) to determine their viability (Figure 10b, upper row).

Consistent with complete scission of the quenched fluorophores, cells remained non-fluorescent in the 647 channel on day 2, with no signal rebound observed. The cells were calcein AM-bright and had increased in density, consistent with unhindered interim proliferation. As a control, we used a conventional TCO-Tz pair that can click for bioorthogonal

quenching but cannot cleave fluorophores from the antibody<sup>83</sup>. Although the cells were again calcein AM-positive and proliferating, a spontaneous increase in fluorescence signal was observed in the absence of scission. Black hole quenchers are known to be vulnerable to azo bond cleavage, particularly *in vivo*<sup>85</sup>; the observed rebound is consistent with slow intracellular and/or extracellular degradation of the BHQ3, leading to loss of quenching and the reappearing signal. While both bioorthogonal methods achieve efficient short-term cycling in living cells, scission is essential for serial profiling in longer timeframes where antibody internalization is expected and fluorescence rebound is a hazard.

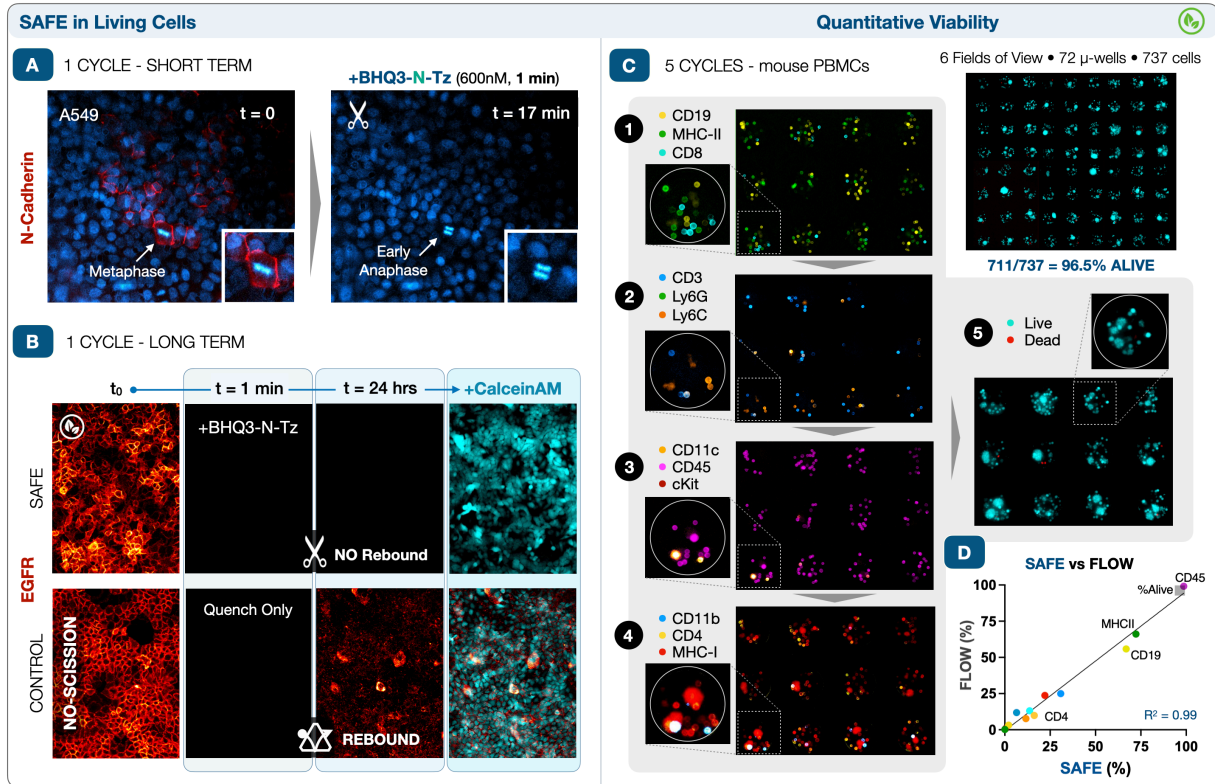


**Figure 10.** (a) Staining and scission with SAFE647-anti-N-Cadherin confirmed efficient scission and short-term nontoxicity in living A549 cells, a subset of which progressed through mitosis during the experiment. (b) Longer term imaging of A549 cells was used to confirm the lack of toxicity and assess the impact of scission. Serial imaging over 24 hours demonstrated durable signal elimination and intact live cell calcein-AM staining. Control cells stained and quenched in parallel with a non-scissile fluorophore-TCO and BHQ3-Tz<sup>83</sup> were initially dark, but exhibited marked rebound of the fluorescent signal 24 hrs later, likely due to extra/intracellular degradation of the BHQ3 quencher, indicating a critical role for scission. (c) To quantify cell viability across multiple cycles of staining and quenching, living mouse PBMCs were isolated, aliquoted, loaded into microwells for imaging. The cells were profiled with a SAFE panel of 12 immune markers, imaged in sets of three, followed by live/dead staining dyes to assess cell survival. Efficient scission performance produced images with high signal to background across all five cycles and no evident residual signal. (d) Both cell viability after bioorthogonal profiling (96.5% vs. 96.2%) and marker abundance matched well with flow cytometry controls ( $R^2=0.99$ ).

We next sought to extend SAFE live cell cycling to multiple cycles of staining and beyond cancer cell lines, in order to validate nontoxicity in mixed populations of primary immune cells. To image living mouse peripheral blood mononuclear cells (PBMCs) in suspension, we fabricated PDMS microwells (80  $\mu\text{m}$  diameter, 80  $\mu\text{m}$  depth) using soft lithography.<sup>86</sup> Both short-term imaging experiments and subsequent cell culture experiments (*vide infra*) were performed with these microwells, which showed excellent retention of the suspended cells, necessary for marker quantitation across cycles. Freshly harvested mouse PBMCs were isolated, pooled, and then loaded into microwells for imaging, reserving aliquots for parallel

analysis by flow cytometry. We visualized 12 targets across 4 cycles of imaging and quenching in live cells over the course of <2 hours of elapsed time. At the end, we determined the cell viability (711 alive / 737 total cells in 72 microwells, 96.5% alive) in a fifth round of imaging with calcein AM/sytox red (Figure 10c). The cells expressing each marker were counted and compared to the aliquot analyzed synchronously by flow cytometry for the same target panel. There was an excellent correlation ( $R^2 = 0.985$ ) between populations measured by SAFE ( $N = 737$ ) and flow cytometry ( $N > 10^5$ ) in both their marker abundance and in the measured cell viability (96.2 vs 96.5%, Figure 10d), confirming i) the staining accuracy across multiple cycles of imaging and scission-mediated fluorophore exchange, ii) the ability to accurately quantify cellular abundance in small/sparse samples, and iii) the lack of toxicity to living PBMCs.

### 3.3 Profiling the Differentiation of Living Bone Marrow

Hematopoietic development generates phenotypic diversity as multipotent stem/progenitor cells differentiate into their repertoire of mature progeny. High-dimensional multiplexed immunohisto-chemical and flow cytometric profiling has mapped developmental hierarchies; likewise, single-cell gene expression analysis and barcoding technologies have traced hematopoietic lineages. Directly visualizing the bone marrow cells and their ensemble of surface markers in the midst of these changes, however, has not been possible. As an initial test of the feasibility of SAFE profiling of living bone marrow, freshly harvested murine bone marrow cells were counted and put into culture overnight. We profiled 12 immune markers (3 markers/cycle, 4 cycles total), with a focus on myeloid precursors (Figure 11a), using confocal imaging to distinguish membrane/cytoplasmic staining. Calcein-AM staining at the end of the profiling sequence confirmed the cellular viability.

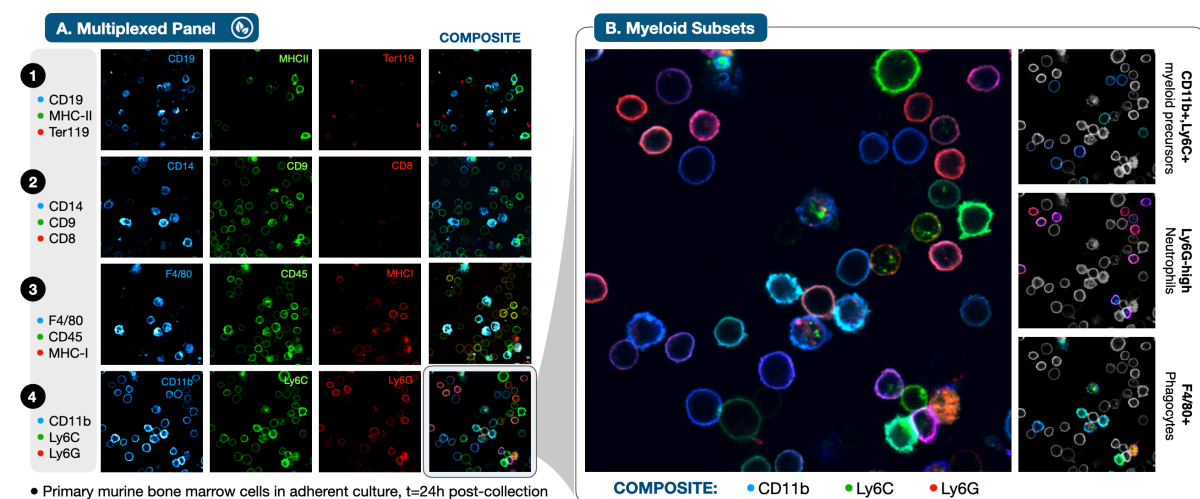


**Figure 11.** (a) Primary murine bone marrow cells were isolated, plated in adherent culture and imaged after 24 hours. Confocal microscopy of twelve markers profiled in 4 cycles enabled discrimination of intracellular and extracellular fluorescent staining at high spatial resolution. A minority of cells displayed intracellular staining that was not removed by scission, suggestive of antibody internalization prior to fluorophore scission with BHQ3-N-Tz. (b) A focus on the myeloid markers in cycle 4 reveals an ensemble of myeloid precursors (CD11b+, Ly6C+), Ly6G-Hi neutrophils, and F4/80+ phagocytes (F4/80+) within the developing bone marrow cell population, highlighted in the selectively (de)colored individual panels at right.

CD8 positive cells were rare, indicating that non-adherent T-cells were not efficiently retained in this staining format. Images demonstrated the presence of erythroid (Ter119+), lymphoid (CD19+) and myeloid (CD11b+) subsets within the population, including cells across a spectrum of functional differentiation. A continuum of CD11b, Ly6C, and Ly6G expression was evident in the high-resolution composite image (Figure 11b), with myeloid precursors (CD11b+, Ly6C+) that render as blue-cyan, and mature Ly6G+ neutrophils that appear magenta-red. A subset of phagocytically-proficient cells (CD14+ and F4/80+ in cycles 2 and 3, respectively) exhibited a pattern of multi-color intracellular staining consistent with antibody internalization prior to scission, in addition to the ON/OFF cycling of specific cell-surface markers. Apart from this subpopulation, negligible cytoplasmic signal was observed after four complete cycles, indicating the feasibility of accurate, iterative staining and scission in this cellular context.

To implement longitudinal bioorthogonal profiling on longer time scales, i.e. across not just multiple cycles but multiple days, we selected a model system with well-defined cellular dynamics. Estrogen-regulated Hoxb8 (ER-Hoxb8) hematopoietic progenitor cells are conditionally immortalized by retroviral infection of neutrophil-committed myeloid bone marrow progenitors<sup>87</sup>. Removal of  $\beta$ -estradiol from culture media triggers the ER-Hoxb8 differentiation program. Cells become mature neutrophils at day 4-6, a developmental sequence that has been well-characterized by flow cytometry and gene expression (Figure 12, inset)<sup>88</sup>. Loss of cKit expression and sequential upregulation of CD11b, Ly6C, and Ly6G occur in tandem with population expansion.

We thus loaded a sparse density of ER-Hoxb8 cells into PDMS microwells (W: 60  $\mu$ m, H: 80  $\mu$ m, Figure 12a), fabricated as in the PBMC studies (*vide supra*). The same cells were imaged longitudinally during differentiation (D0, D2, D4, D6) in two profiling cycles at each time point, staining for CD45 and F4/80 as positive/negative controls, respectively, in addition to the quartet of differentiation markers. At D0, all cells were CD45+/cKit+ and negative for the remaining panel, as expected. Rapid population growth by D2 tracked with broad upregulation of CD11b and a subset of Ly6C positive cells. The density of viable cells peaked on D4, concomitantly with the appearance of bright Ly6G staining. Given the short lifespan of differentiated granulocytes<sup>89</sup>, population density had decreased slightly by D6, consistent with the fraction of dead cells normally observed by flow cytometry. F4/80 staining remained negative throughout, as expected for differentiation under these neutrophil-selective culture conditions. Cell growth during temporospatial profiling was robust, allowing quantitative analysis of both proliferation and differentiation across the individual microwells (Figure 12b).

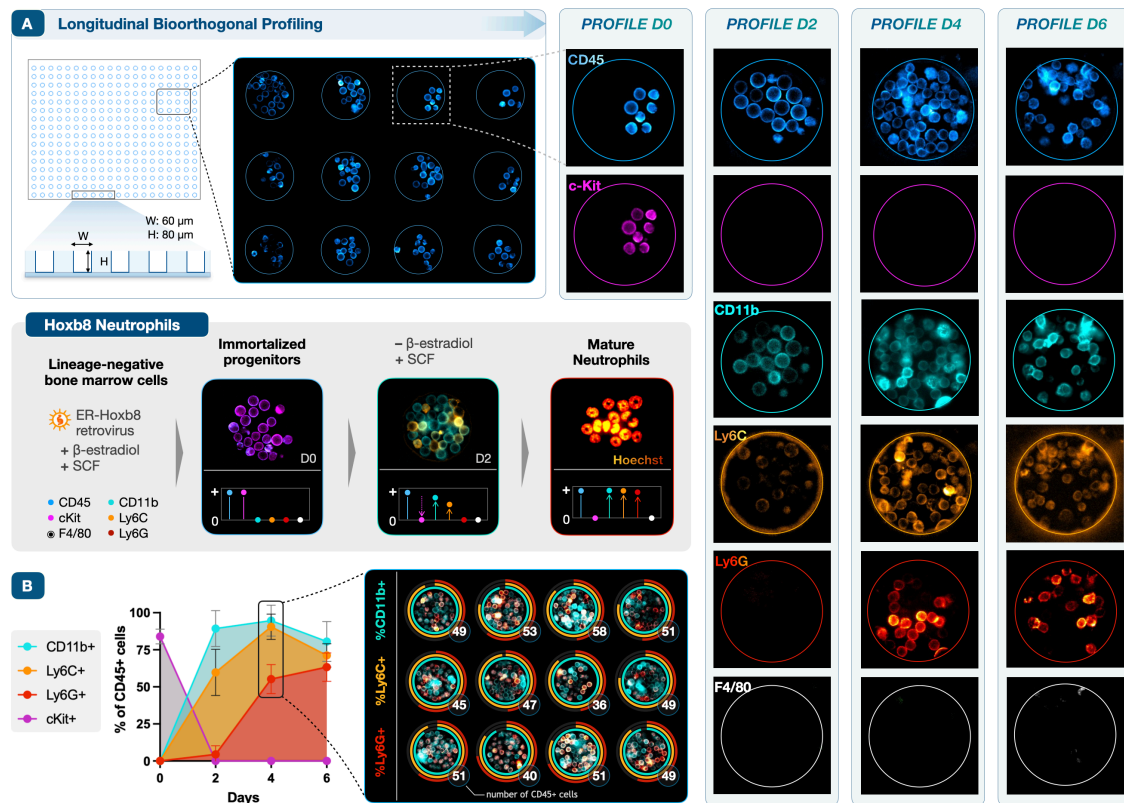


**Figure 12.** (a) Deep PDMS microwells efficiently retain suspension cells in culture for serial imaging. Bone marrow derived ER-Hoxb8 cells are conditionally immortalized when cultured with  $\beta$ -estradiol; removal of  $\beta$ -estradiol triggers synchronous expansion and neutrophilic differentiation. The developmental sequence induces broad changes in extracellular marker expression and cellular morphology (gray panel, inset). To track this process, CD45, cKit, CD11b, Ly6C, Ly6G, and F4/80 were serially profiled at days 0, 2, 4, and 6, before and during differentiation. CD45 (positive control) and F4/80 (negative control) expression were stable, while cKit (a progenitor cell marker) expression rapidly decreased, disappearing after D0. As expected, the fraction of cells expressing CD11b, Ly6C, and Ly6G rose in sequence over the first 4-6 days. (b) Quantitative expression of differentiation markers across six days and four profiles: (i) averaged across a set of 12 microwells; (ii) quantified on day 4 to track proliferation and variation across individual wells. Ring plots track marker expression (fraction of positive cells, encoded by color) and the total number of CD45+ cells per well (in white).

## 4. Discussion

During my research stay at the Center for Systems Biology (Massachusetts General Hospital and Harvard Medical School) we created a new method for multiplexed longitudinal profiling of live cells, to demonstrate 14 color imaging in living primary hematopoietic and immune populations, across a timescale spanning minutes to days. Methods that incorporate multiple cycles of fluorescent staining and quenching were originally developed for paraffin-embedded tissue sections that can withstand harsh destaining conditions<sup>63,90,91</sup>. The recent method for immunostaining with Tz/TCO-driven bioorthogonal quenching<sup>83,92</sup> achieves its speed by circumventing the need to remove fluorophores. While capable of rapid temporal cycling at nontoxic reagent concentrations, the quenching is reversed by biochemical degradation over longer timeframes in living systems, leading to signal rebound. In contradistinction, the SAFE method bypasses the above shortcomings and allows extremely fast cycling in the seconds time frame (>99% signal clearance in <30 sec), while using very low concentrations of reagents for gentle and irreversible fluorophore scission. To the best of our knowledge, this developed

approach is currently the only technique that allows such temporospatial profiling in living cells.

Bioorthogonal reactions have long been described in live cells as an alternative route to biomolecular tagging<sup>3</sup>, with incorporation of functionalized noncanonical amino acids into proteins<sup>93,94</sup>, modified nucleosides into DNA/RNA<sup>95</sup>, metabolic building blocks into glycans<sup>96</sup>, or clickable tags into chemical probes<sup>97,98</sup>, followed by subsequent click-mediated labeling. The impetus for developing these strategies has primarily been visualization of the different classes of biomolecules in living systems, exploiting the small footprint of compact chemical tags to follow biological trafficking<sup>96</sup> or create a readout for replication/metabolism<sup>95</sup>. Such tags have also featured in strategies for super resolution microscopy<sup>99-101</sup>. Here, we apply chemical tools not to deliver labels but rather to remove them via bioorthogonal bond cleavage<sup>38,102</sup>, pursuing highly multiplexed temporal analysis of cell-surface protein expression. We utilized a new generation of cleavable linkers based on a new scaffold (C<sub>2</sub>TCO) and optimized acid-functionalized tetrazine-scissors—the first bioorthogonal reagents capable of achieving both complete (>99.5%) and rapid (seconds) scission<sup>50</sup>. Simultaneously, the superb stability of C<sub>2</sub>TCO (>97% at 48 hrs) is critical to maintaining ultra-efficient cleavage over time. By accelerating the scission sequence with the cooperative BHQ3-fluorophore-driven click kinetics, the SAFE reagents achieve a unique combination of intrinsic biochemical stability and high reactivity that arises as an emergent property of the system.

The proof-of principle experiments shown here could be further expanded to increase the number of cycles with each profile and/or to broaden the number of proteins that are simultaneously detectable. One of the key advantages of the SAFE method is that the underlying bioorthogonal scission reaction is compatible with any conjugatable dye, including polymeric fluorochromes (e.g. BV dye series) that are otherwise difficult to quench. Since a range of bright polymer dyes can be excited in the violet/UV, their use together with organic rhodamine/cyanine dyes could enable broader multiplexing to ~8 channels per cycle with minimal spectral overlap. Over 10 cycles (feasible with observed scission efficiencies >99.5%), this would allow analysis of up to 80 protein biomarkers in live cells. Finally, while our focus here was on temporospatial analysis of living cells in culture, the above approaches are entirely compatible with fixed cell and tissue analyses, expanding the analytical capabilities of clinical sample testing. This in turn has potential applications for deeper immune cell profiling, single cell pathway analysis, and drug response testing in biopsy samples, as well as opening the door to multiplexed functional profiling of living cells and tissues after explantation or even *in vivo*.

## 5. Experimental Methods

Hereinafter, all synthetic methods, characterizations, probe activations and approaches for kinetic measurements carried out at the home institution within this research project are described in detail.

### 5.1 Synthesis and Characterization

Unless otherwise noted, reactions were carried out under an atmosphere of argon in air-dried glassware with magnetic stirring. Air- and/or moisture-sensitive liquids were transferred via syringe. All reagents were purchased from commercial sources without further purification. Dichloromethane, methanol, THF and diethyl ether were dried using PURESOLV-columns (Inert Corporation, USA). Solvents used for flash column chromatography were purchased from Donau Chemie AG (Austria). Dry acetonitrile and dry DMF were obtained from Sigma-Aldrich (Germany) and ACROS Organics (Belgium), respectively, and stored under argon. Thin layer chromatography was performed using TLC plates on aluminum support (Merck, silica gel 60, fluorescent indicator 254). Column chromatography was performed using a BUCHI Sepacore Flash System (2 x BUCHI Pump Module C-605, BUCHI Pump Manager C-615, BUCHI UV Photometer C-635, and BUCHI Fraction Collector C-660) and a Reveleris® X2 Flash Chromatography/Prep Purification Systems (BUCHI). Silica gel 60 (40-63  $\mu\text{m}$ ) was obtained from Merck. A Kinetex® 5  $\mu\text{m}$  C18 100 Å, AXIA LC column (100 x 30.0 mm, Phenomenex) was used for preparative HPLC. HPLC grade solvents were purchased from VWR (USA).

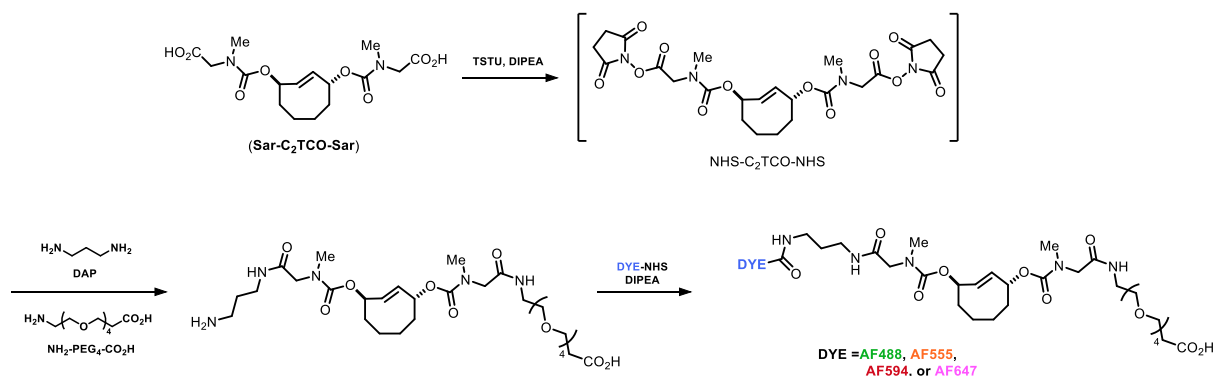
$^1\text{H}$  and  $^{13}\text{C}$  NMR spectra were recorded on a Bruker AC 200 MHz, Bruker Avance UltraShield 400 MHz or Bruker Ascend 600 MHz spectrometer at 20 °C. Chemical shifts are reported in ppm ( $\delta$ ) relative to tetramethylsilane and calibrated using solvent residual peaks. Data is shown as follows: Chemical shift, multiplicity (s = singlet, d = doublet, t = triplet, q = quartet, quint = quintet, m = multiplet, b = broad signal), coupling constants ( $J$ , Hz) and integration. HPLC analysis was performed on a Nexera X2® UHPLC system (Shimadzu®) comprised of LC-30AD pumps, SIL-30AC autosampler, CTO-20AC column oven and DGU-20A<sub>5/3</sub> degasser module. Detection was done using an SPD-M20A photo diode array, an RF-20Ax fluorescence detector, and ELS-2041 evaporative light scattering detector (JASCO®) and an LCMS-2020 mass spectrometer (ESI/APCI). If not stated otherwise, all separations were performed using a Waters® XSelect® CSH™ C18 2,5  $\mu\text{m}$  (3.0 x 50 mm) column XP at 40 °C, and a flowrate of 1.7 mL/min with water/acetonitrile + 0.1% formic acid gradient elution.

HRMS analysis was carried out using methanol solutions (concentration: 10 ppm) on an Agilent 6230 LC TOFMS mass spectrometer equipped with an Agilent Dual AJS ESI-Source. The mass spectrometer was connected to a liquid chromatography system of the 1100/1200 series from Agilent Technologies (Palo Alto, CA, USA). The system consisted of a 1200SL binary gradient pump, a degasser, column thermostat, and an HTC PAL autosampler (CTC Analytics AG, Zwingen, Switzerland).

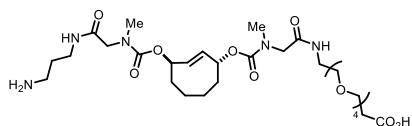
Fluorescence measurements were conducted with a PTI QuantaMaster 400 fluorimeter (Photon Technologies Incorporated, NJ, USA) equipped with a Pelletier apparatus for temperature control, multi-sample changer with integrated magnetic stirring, and a sample

addition port for continuous kinetic measurements. UV-VIS absorption spectra were measured on a Horiba DualFL spectrophotometer (Horiba Instruments, NJ, USA) or Nandrop Spectrophotometer (ThermoFisher).

### Synthesis of fluorogenic C<sub>2</sub>TCO probes



### DAP-C<sub>2</sub>TCO-PEG<sub>4</sub>-COOH



Sar-C<sub>2</sub>TCO-Sar (147 mg, 0.39 mmol) was dissolved in dry DMSO (1 mL) and a solution of TSTU (261 mg, 0.87 mmol) in dry DMSO (1 mL) and DIPEA (444  $\mu$ L, 2.57 mmol) were added.

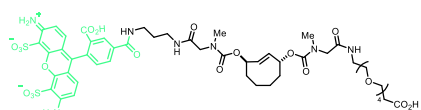
The mixture was stirred at room temperature for 90 min until LCMS showed full conversion (after quenching a sample by addition of an excess of 2-(2-aminoethoxy)ethanol). A solution of NH<sub>2</sub>-PEG<sub>4</sub>-COOH (34.6 mg, 0.13 mmol) suspended in dry DMSO (300  $\mu$ L) was added and the mixture was stirred at room temperature for 150 min until LCMS showed full conversion (after quenching a sample with an excess of 1,3-diaminopropane (DAP)). The mixture was quenched with formic acid (315  $\mu$ L) while cooling in an ice bath, diluted with water (2 mL) and directly loaded onto a C18 column. Preparative reversed phase column chromatography (H<sub>2</sub>O/MeCN gradient elution, 0.1% formic acid) gave the desired product as a pale-yellow oil (40.5 mg, 47%); <sup>1</sup>H NMR (600 MHz, DMSO-*d*<sub>6</sub>, mixture of rotamers)  $\delta$  8.43-7.99 (m, 3H), 5.79 (t, *J* = 37 Hz, 2H), 5.25 (t, *J* = 31 Hz, 2H), 3.89-3.77 (6H), 3.57-3.42 (14H), 3.22-3.07 (5H), 2.97-2.71 (9H), 2.38-2.25 (2H), 1.95 (dd, *J* = 47 Hz, 11.7 Hz, 2H), 1.78-1.46 (m, 7H), 1.15-0.84 (m, 2H); <sup>13</sup>C NMR (151 MHz, DMSO-*d*<sub>6</sub>, mixture of rotamers)  $\delta$  173.7, 170.5, 169.0, 168.8, 168.7, 168.3, 165.7, 155.1, 154.8, 154.7, 129.9, 129.7, 129.6, 129.5, 129.4, 73.7, 69.80, 69.77, 69.74, 69.62, 69.53, 69.1, 69.0, 67.3, 67.2, 66.8, 51.3, 40.4, 38.6, 36.7, 36.6, 36.5, 36.22, 36.18, 35.7, 35.2, 35.1, 29.3, 27.8, 23.4, 23.3, 23.2, 21.1; ESI-MS [M+H]<sup>+</sup> *m/z* calcd. 676.38 for C<sub>24</sub>H<sub>42</sub>N<sub>5</sub>O<sub>9</sub><sup>+</sup>, found 676.31.

### General procedure for fluorogenic C<sub>2</sub>TCO probes

DAP-C<sub>2</sub>TCO-PEG<sub>4</sub>-COOH (1 eq.) was dissolved in dry DMSO (50  $\mu$ L/ $\mu$ mol TCO) and a solution of Dye-NHS ester (1.2 eq.) in dry DMSO (500  $\mu$ L) and DIPEA (4 eq.) were added. The reaction mixture was stirred at room temperature under argon-atmosphere until LCMS showed full conversion. The mixture was diluted with aq. ammonium formate buffer (1 mL, 2.5 mM, 9.2

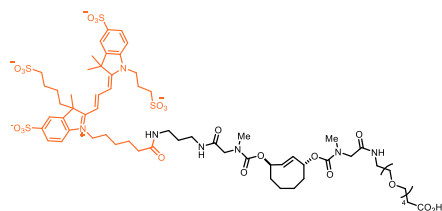
pH) and directly loaded onto a C18 column. The crude product was purified by preparative reversed phase column chromatography (ammonium formate buffer (2.5 mM, 9.2 pH)/MeCN gradient elution) to give desired Dye-C<sub>2</sub>TCO-PEG<sub>4</sub>-COOH adduct. To get rid of excess ammonium formate salt in the product mixture, the colorful residue was dissolved in neutral water (1.5 mL), loaded onto a 12 g Biotage Snap C18 Ultra column, and flushed with 100% water for 20 min. The product was obtained by elution with 95% MeCN in neutral water. NMR spectroscopy for each substance was measured prior to desalting.

### AF488-C<sub>2</sub>TCO-PEG<sub>4</sub>-COOH



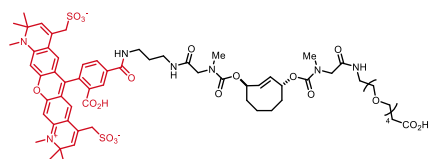
Synthesis was performed according to the general procedure using DAP-C<sub>2</sub>TCO-PEG<sub>4</sub>-COOH (5.75 mg, 8.5 μmol), AF488-NHS (6.45 mg, 10.2 μmol) and DIPEA (5.9 μL, 34 μmol). The desired product was obtained after desalting protocol as an orange oil (7.7 mg, 76%); <sup>1</sup>H NMR (600 MHz, D<sub>2</sub>O, mixture of rotamers) δ 8.32 (s, 1H), 8.01 (d, *J* = 8.0 Hz, 1H), 7.45 (d, *J* = 8.2 Hz, 1H), 7.22-7.18 (m, 2H), 6.96 (d, *J* = 9.3 Hz, 2H), 5.99-5.56 (m, 2H), 5.45-5.22 (m, 2H), 4.15-3.85 (m, 4H), 3.81-3.34 (m, 24H), 3.21-2.88 (m, 7H), 2.72 (s, 1H), 2.55 (t, *J* = 6.3 Hz, 2H), 2.15-1.56 (m, 9H), 1.42-1.08 (m, 3H), 0.98-0.83 (bs, 1H); ESI-MS [M-H]<sup>-</sup> *m/z* calcd. 1190.36 for C<sub>51</sub>H<sub>64</sub>N<sub>6</sub>N<sub>7</sub>O<sub>22</sub>S<sub>2</sub><sup>-</sup>, found 1190.40.

### AF555-C<sub>2</sub>TCO-PEG<sub>4</sub>-COOH



Synthesis was performed according to the general procedure using DAP-C<sub>2</sub>TCO-PEG<sub>4</sub>-COOH (5 mg, 7.4 μmol), AF555-NHS (8.4 mg, 8.9 μmol) and DIPEA (5.2 μL, 29.6 μmol). The desired product was obtained after desalting protocol as a purple oil (7.5 mg, 68%); <sup>1</sup>H NMR (600 MHz, D<sub>2</sub>O, mixture of rotamers) δ 8.57 (t, *J* = 13.7 Hz, 1H), 8.44 (s, 1H), 7.95 (s, 1H), 7.88 (t, *J* = 9.6 Hz, 3H), 7.45 (t, *J* = 7.7 Hz, 2H), 6.51 (t, *J* = 14.1 Hz, 2H), 5.93-5.57 (m, 2H), 5.40-5.22 (m, 2H), 4.31 (t, *J* = 7.2 Hz, 2H), 4.20 (t, *J* = 7.2 Hz, 2H), 4.02-3.84 (m, 4H), 3.75 (t, *J* = 6.4 Hz, 2H), 3.67-3.60 (m, 15H), 3.41 (t, *J* = 4.8 Hz, 2H), 3.16-3.06 (m, 6H), 3.00-2.92 (m, 6H), 2.69 (t, *J* = 8.3 Hz, 2H), 2.52 (t, *J* = 8.2 Hz, 2H), 2.47-2.23 (m, 7H), 2.06-1.87 (m, 4H), 1.80-1.77 (m, 10H), 1.68-1.57 (m, 11H), 1.39-1.30 (m, 3H), 1.08-1.04 (m, 2H), 0.89-0.78 (m, 2H); ESI-MS [(M+H)/2]<sup>+</sup> *m/z* calcd. 752.27 for [C<sub>65</sub>H<sub>97</sub>N<sub>7</sub>O<sub>25</sub>S<sub>4</sub>]<sup>+</sup>/2, found 752.15.

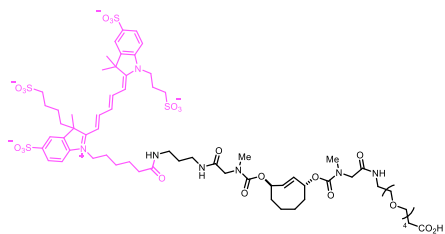
### AF594-C<sub>2</sub>TCO-PEG<sub>4</sub>-COOH (XX)



Synthesis was performed according to the general procedure using DAP-C<sub>2</sub>TCO-PEG<sub>4</sub>-COOH (5.75 mg, 8.5 μmol), AF594-NHS (8.4 mg, 10.2 μmol) and DIPEA (5.9 μL, 34 μmol). The desired product was obtained after desalting protocol as a dark purple oil (8.5 mg, 72%); <sup>1</sup>H NMR (600 MHz, D<sub>2</sub>O, mixture of rotamers) δ 8.34 (s, 1H), 8.05-8.01 (m, 1H), 7.42-7.7.40 (m, 1H), 7.12-7.10 (m, 2H), 6.69-6.66 (m, 2H), 5.98-5.74 (m, 4H), 5.35-5.21 (m, 2H), 4.06-3.79 (m, 7H), 3.74 (t, *J* = 6.2 Hz, 2H), 3.69-3.48 (m, 20H),

3.42-3.32 (m, 4H), 3.08-2.92 (m, 13H), 2.72 (s, 0.5H), 2.54 (t,  $J = 6.3$  Hz, 2H), 2.20-1.60 (m, 9H), 1.50 (s, 13H), 1.39-1.26 (m, 0.5H), 1.21-1.10 (m, 0.5H), 0.99-0.81 (m, 1.5); ESI-MS  $[M+H]^+$   $m/z$  calcd. 1380.53 for  $C_{65}H_{86}N_6N_7O_{22}S_2^+$ , found 1380.55.

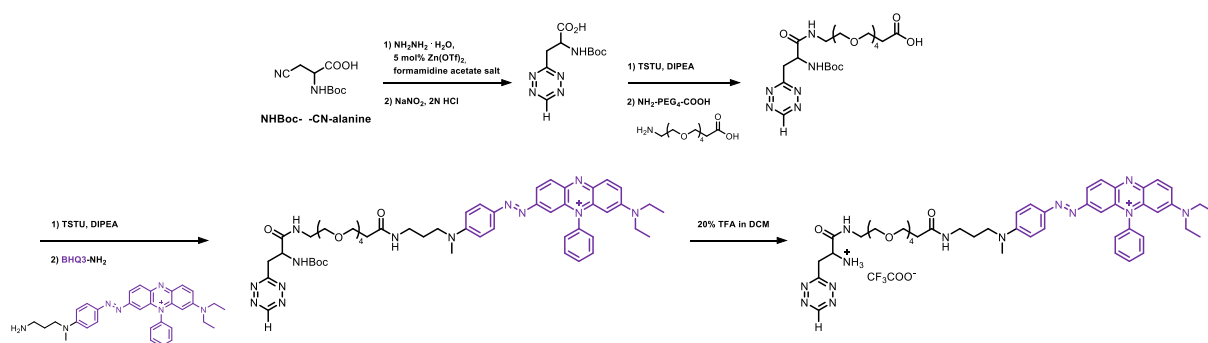
### AF647-C<sub>2</sub>TCO-PEG<sub>4</sub>-COOH



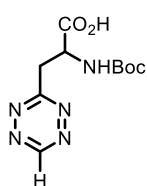
Synthesis was performed according to the general procedure using DAP-C<sub>2</sub>TCO-PEG<sub>4</sub>-COOH (4 mg, 5.9  $\mu$ mol), AF647-NHS (6.9 mg, 7.1  $\mu$ mol) and DIPEA (4.2  $\mu$ L, 23.7  $\mu$ mol). The desired product was obtained after desalting protocol as a blue oil (6.2 mg, 68%); <sup>1</sup>H NMR (600 MHz, D<sub>2</sub>O, mixture of rotamers)  $\delta$  8.13 (q,  $J = 13.6$  Hz, 2H), 7.90-

7.84 (m, 4H), 7.37 (dd,  $J = 24.2$  Hz,  $J = 8.9$  Hz, 2H), 6.67 (t,  $J = 12.2$  Hz, 1H), 6.42 (d,  $J = 13.2$  Hz, 2H), 5.92-5.70 (m, 2H), 5.26-5.21 (m, 2H), 4.26 (bs, 2H), 4.16 (bs, 2H), 4.04-3.84 (m, 4H), 3.75 (t,  $J = 6.3$  Hz, 2H), 3.68-3.58 (m, 15H), 3.39 (bs, 2H), 3.16-2.92 (m, 12.5H), 2.72-2.68 (m, 3.5H), 2.38-2.21 (m, 6H), 2.02-1.84 (m, 4H), 1.72-1.50 (m, 20H), 1.35 (bs, 2H), 0.99 (bs, 1H), 0.87 (m, 1H), 0.71 (bs, 1H); ESI-MS  $[M+H]^+$   $m/z$  calcd. 1530.56 for  $C_{67}H_{100}N_7O_{25}S_4^+$ , found 1530.50.

### Synthesis of H-HK-BHQ3

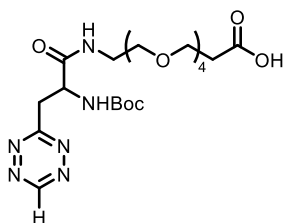


### H-NHBocAla



To a well-blended mixture of NHBoc- $\beta$ -CN-alanine (600 mg, 2.8 mmol), formamidine acetate salt (1.46 g, 14 mmol) and  $Zn(OTf)_2$  (255 mg, 0.7 mmol) dry dioxane (8.4 mL, 98 mmol) and hydrazine monohydrate (6.8 mL, 140 mmol) were added at room temperature and the vial was sealed immediately. The reaction mixture was stirred at 30 °C for 72 h after which it was poured onto ice-water (50 mL). After addition of  $NaNO_2$  (3.9 g, 56 mmol) the solution was acidified with aqueous 2N HCl solution (60 mL). The mixture was extracted with EtOAc (5 x 70 mL), the combined organic layer was dried over  $MgSO_4$ , filtered and concentrated. Purification was performed by preparative reversed phase column chromatography (C18, H<sub>2</sub>O/MeCN, gradient elution, 0.1% formic acid) to afford the desired product (35.4 mg, 5%) as a pink oil; <sup>1</sup>H-NMR (600 MHz, CD<sub>3</sub>OD)  $\delta$  10.33 (s, 1H), 4.81 (dd,  $J = 7.5$  Hz, 5.9 Hz, 1H), 3.90 (dd,  $J = 14.8$  Hz, 5.6 Hz, 1H), 3.67 (dd,  $J = 15.2$  Hz, 8.8 Hz, 1H), 1.37 (s, 9H); <sup>13</sup>C NMR (151 MHz, CD<sub>3</sub>OD)  $\delta$  173.9, 171.4, 159.4, 157.6, 80.7, 53.6, 38.9, 28.6; ESI-MS  $[M+H]^+$  calcd. 270.12 for  $C_6H_9N_4O_2^+$  found 270.10;

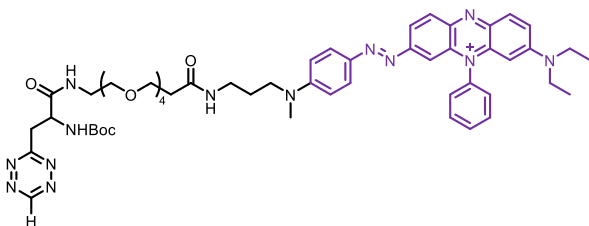
### H-NHBocAla-PEG<sub>4</sub> acid



H-NHBocAla (4 mg, 14.9  $\mu\text{mol}$ ) was dissolved in dry DMSO (250  $\mu\text{L}$ ), and TSTU (5.4 mg, 17.8  $\mu\text{mol}$ ) and DIPEA (5.2  $\mu\text{L}$ , 29.7  $\mu\text{mol}$ ) were added. The mixture was stirred at room temperature for 40 min.  $\text{NH}_2\text{-PEG}_4\text{-COOH}$  (7.9 mg, 29.7  $\mu\text{mol}$ ) suspended in dry DMSO (300  $\mu\text{L}$ ) was added and stirring was continued for 1.5 h. The reaction mixture was quenched with 1% formic acid in water (900  $\mu\text{L}$ ) while cooling in an ice

bath. Purification by reversed phase column chromatography ( $\text{H}_2\text{O}/\text{MeCN}$  gradient elution, 0.1% formic acid) afforded the desired product as a red oil (4.9 mg, 65%);  $^1\text{H}$  NMR (400 MHz,  $\text{CD}_3\text{OD}$ )  $\delta$  10.34 (s, 1H), 4.75 (dd,  $J = 8.3$  Hz, 5.8 Hz, 1H), 3.83 (dd,  $J = 14.4$  Hz, 5.2 Hz, 1H), 3.73 (t,  $J = 6.2$  Hz, 2H), 3.65-3.53 (m, 18H), 3.38 (q,  $J = 4.6$  Hz, 2H), 2.53 (t,  $J = 6.0$  Hz, 2H), 1.37 (s, 9H);  $^{13}\text{C}$  NMR (101 MHz,  $\text{CD}_3\text{OD}$ )  $\delta$  176.4, 172.8, 171.5, 157.4, 80.9, 71.57, 71.54, 71.46, 71.4, 71.2, 70.4, 68.1, 54.7, 40.5, 39.2, 36.3, 28.6; ESI-MS  $[\text{M}+\text{H}]^+$   $m/z$  calcd. 517.26 for  $\text{C}_{21}\text{H}_{37}\text{N}_6\text{O}_9^+$ , found 517.46.

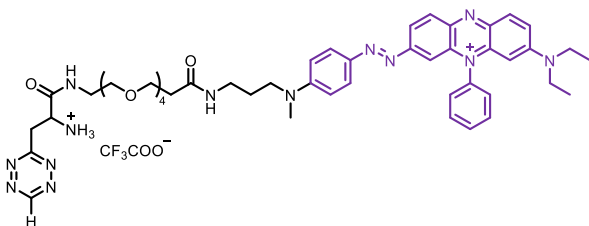
### H-NHBocAla-PEG<sub>4</sub>-BHQ3



H-NHBocAla-PEG<sub>4</sub> acid (4.9 mg, 9.49  $\mu\text{mol}$ ) was dissolved in dry DMSO (260  $\mu\text{L}$ ) and TSTU (3.4 mg, 11.4  $\mu\text{mol}$ ) and DIPEA (3.3  $\mu\text{L}$ , 18.9  $\mu\text{mol}$ ) were added. The mixture was stirred at room temperature for 30 min. BHQ3-amine (5 mg, 9.6  $\mu\text{mol}$ ) dissolved in dry DMSO (300

$\mu\text{L}$ ) was added and stirring was continued for 2 h. The reaction mixture was quenched with formic acid (15  $\mu\text{L}$ ) and 0.1% formic acid in water (900  $\mu\text{L}$ ) while cooling in an ice bath. Purification by reversed phase column chromatography (10 mM ammonium formate buffer pH 9 /  $\text{MeCN}$  gradient elution) afforded the desired product as a dark blue solid (5.95 mg, 62%);  $^1\text{H}$  NMR (400 MHz,  $\text{CD}_3\text{OD}$ )  $\delta$  10.30 (s, 1H), 8.40-8.12 (m, 3H), 7.97-7.91 (m, 4H), 7.80 (bs, 2H), 7.69 (d,  $J = 7.2$  Hz, 2H), 7.37 (bs, 1H), 6.86 (d,  $J = 9.2$  Hz, 2H), 5.90 (bs, 1H), 4.69 (dd,  $J = 8.4$  Hz, 5.8 Hz, 1H), 3.81-3.73 (m, 3H), 3.62-3.55 (m, 16H), 3.48 (t,  $J = 5.6$  Hz, 2H), 3.35-3.33 (m, 1H), 3.27 (t,  $J = 6.5$  Hz, 2H), 2.45 (t,  $J = 5.9$  Hz, 2H), 2.19 (q,  $J = 7.1$  Hz, 3H), 1.86 (quin,  $J = 7.0$  Hz, 2H), 1.60 (bs, 3H), 1.38-1.29 (m, 15H), 1.22-1.00 (m, 4H), 0.90 (t,  $J = 6.5$  Hz, 1H); ESI-MS  $[\text{M}+\text{H}]^+$   $m/z$  calcd. 1014.53 for  $\text{C}_{53}\text{H}_{68}\text{N}_{13}\text{O}_8^+$ , found 1014.56.

### BHQ3-N-Tz (2)



H-NHBocAla-PEG<sub>4</sub>-BHQ3 (3 mg, 2.95  $\mu\text{mol}$ ) was dissolved in dry DCM (1 mL) and TFA (200  $\mu\text{L}$ ) was added dropwise. The solution was stirred at room temperature for 40 min until LCMS indicated complete deprotection. The reaction mixture was diluted with

$\text{MeCN}/\text{DCM}$  (1:1, 2 mL), concentrated under reduced pressure and the residue was co-

evaporated with MeCN three more times (1.5 mL each) to give the desired product as a dark blue oil (2.7 mg, >99%);  $^1\text{H}$  NMR (400 MHz,  $\text{CD}_3\text{OD}$ )  $\delta$  8.38 (d,  $J = 9.3$  Hz, 1H), 8.25 (d,  $J = 9.2$  Hz, 1H), 8.16 (d,  $J = 9.9$  Hz, 1H), 7.97-7.91 (m, 4H), 7.81 (d,  $J = 9.3$  Hz, 2H), 7.68 (d,  $J = 7.5$  Hz, 2H), 7.39 (s, 1H), 6.85 (d,  $J = 9.1$  Hz, 2H), 5.90 (d,  $J = 2.2$  Hz, 1H), 5.34 (t,  $J = 4.8$  Hz, 0.5H), 4.57 (dd,  $J = 7.7$  Hz, 5.4 Hz, 0.5H), 3.93-3.82 (m, 3H), 3.74 (t,  $J = 5.8$  Hz, 3H), 3.64-3.57 (m, 15H), 3.26 (t,  $J = 6.6$  Hz, 2H), 3.14 (s, 3H), 2.46 (t,  $J = 5.9$  Hz, 2H), 2.28 (t,  $J = 7.0$  Hz, 2H), 2.19 (t,  $J = 7.4$  Hz, 2H), 1.86 (t,  $J = 6.2$  Hz, 2H), 1.60 (bs, 3H), 1.16 (d,  $J = 8.3$  Hz, 3H), 0.92-0.87 (m, 6H); ESI-MS  $[\text{M}+\text{H}]^+$   $m/z$  calcd. 917.50 for  $\text{C}_{48}\text{H}_{63}\text{N}_{13}\text{O}_6^{2+}$ , found 917.82.

## 5.2 Probe Activation

To a 500  $\mu\text{L}$  eppendorf tube containing 10-30  $\mu\text{L}$  of DYE- $\text{C}_2\text{TCO}$ -PEG<sub>4</sub>-COOH in anhydrous DMSO were added 2 equivalents of DIPEA followed by 4 equivalents of N,N,N',N'-Tetramethyl-O-(N-succinimidyl)uronium tetrafluoroborate (TSTU) and the solution was quickly vortexed after capping the tube. After one minute, 5 equivalents of 4-(ethylamino)-butanoic acid hydrochloride<sup>51</sup> were added followed by an additional 5 equivalents of DIPEA. Note: The reaction time prior to addition of ENBA is concentration dependent and may be complete in as little as 10 seconds at higher dye/TSTU concentrations. For a dye solution between 1-2 mM, the sixty second reaction time provides optimal discrimination between the PEG<sub>4</sub> carboxylic acid and the rhodamine 2'-carboxylic acid, with minimal conversion to the double-NHS species. After addition of ENBA, the solution was again vortex-mixed and ready to use for protein labeling or LCMS analysis after thirty seconds. The chemistry is moderately moisture sensitive due to the risk of NHS hydrolysis and appropriate storage/handling conditions were applied.

## 5.3 Click and Scission Kinetics

A stock solution of BHQ3-N-Tz was prepared in DMSO at a concentration of 5 mM, verified by absorbance measurements (extinction coefficient  $42,700\text{M}^{-1}\text{cm}^{-1}$  in PBS pH 7.3) and subsequently diluted as needed in small aliquots to prepare a working solution at 250  $\mu\text{M}$ . In parallel, cetuximab (Erbix) was labeled with TSTU-activated AF647- $\text{C}_2\text{TCO}$  to prepare a SAFE647 conjugate with a DOL of 2.6. To a disposable polystyrene cuvette containing 2 mL of PBS and a magnetic stirring bar were then added 40  $\mu\text{L}$  of unlabeled cetuximab (2 mg/mL) to block nonspecific adsorption (40  $\mu\text{g}/\text{mL}$ , 275 nM), followed by 1  $\mu\text{L}$  of the SAFE647-conjugated cetuximab (2040-fold dilution, 6 nM final concentration). Fluorescence intensity was measured (ex 645nm, em 670 nm, monochromator slits 5 nm) to establish a stable background, the baseline intensity of the SAFE labeled antibody, and the time course of click/scission in a continuous trace. After measuring the initial signal, a micropipette was used to inject 8, 10, or 12  $\mu\text{L}$  of BHQ3-N-Tz (250 mM) through the QM400 sample addition port into the stirred cuvette. Nonlinear fitting to a double exponential model in GraphPad Prism 9 (GraphPad software, LLC) was used to calculate a pseudo first order rate constant for the click reaction (falling signal) and a first order rate for the subsequent scission/cleavage (rising signal phase).

## 6. References

1. Dube, D.H. & Bertozzi, C.R. Metabolic oligosaccharide engineering as a tool for glycobiology. *Curr. Opin. Chem. Biol.* **7**, 616-625 (2003).
2. Prescher, J.A., Dube, D.H. & Bertozzi, C.R. Chemical remodelling of cell surfaces in living animals. *Nature* **430**, 873-877 (2004).
3. Prescher, J.A. & Bertozzi, C.R. Chemistry in living systems. *Nat. Chem. Biol.* **1**, 13-21 (2005).
4. Sletten, E.M. & Bertozzi, C.R. Bioorthogonal chemistry: fishing for selectivity in a sea of functionality. *Angew. Chem. Int. Ed. Engl.* **48**, 6974-6998 (2009).
5. Jewett, J.C. & Bertozzi, C.R. Cu-free click cycloaddition reactions in chemical biology. *Chem. Soc. Rev.* **39**, 1272-1279 (2010).
6. Boyce, M. & Bertozzi, C.R. Bringing chemistry to life. *Nat. Methods* **8**, 638-642 (2011).
7. Sletten, E.M. & Bertozzi, C.R. From Mechanism to Mouse: A Tale of Two Bioorthogonal Reactions. *Acc. Chem. Res.* **44**, 666-676 (2011).
8. Carell, T. et al. M. Vrabel and T. Carell for Cycloadditions in Bioorthogonal Chemistry. *Top. Curr. Chem.* **374**, 15 (2016).
9. Saxon, E. & Bertozzi, C.R. Cell Surface Engineering by a Modified Staudinger Reaction. *Science* **287**, 2007-2010 (2000).
10. Chang, P.V., Prescher, J.A., Hangauer, M.J. & Bertozzi, C.R. Imaging Cell Surface Glycans with Bioorthogonal Chemical Reporters. *J. Am. Chem. Soc.* **129**, 8400-8401 (2007).
11. Patterson, D.M., Nazarova, L.A. & Prescher, J.A. Finding the Right (Bioorthogonal) Chemistry. *ACS Chem. Biol.* **9**, 592-605 (2014).
12. Kolb, H.C., Finn, M.G. & Sharpless, K.B. Click chemistry: diverse chemical function from a few good reactions. *Angew. Chem., Int. Ed.* **40**, 2004-2021 (2001).
13. Rostovtsev, V.V., Green, L.G., Fokin, V.V. & Sharpless, K.B. A Stepwise Huisgen Cycloaddition Process: Copper(I)-Catalyzed Regioselective "Ligation" of Azides and Terminal Alkynes. *Angew. Chem. Int. Ed.* **41**, 2596-2599 (2002).
14. Tornøe, C.W., Christensen, C. & Meldal, M. Peptidotriazoles on Solid Phase: [1,2,3]-Triazoles by Regiospecific Copper(I)-Catalyzed 1,3-Dipolar Cycloadditions of Terminal Alkynes to Azides. *J. Org. Chem.* **67**, 3057-3064 (2002).
15. Baskin, J.M. et al. Copper-free click chemistry for dynamic in vivo imaging. *Proc. Natl. Acad. Sci. U.S.A.* **104**, 16793-16797 (2007).
16. Agard, N.J., Prescher, J.A. & Bertozzi, C.R. A strain-promoted [3 + 2] azide-alkyne cycloaddition for covalent modification of biomolecules in living systems. *J. Am. Chem. Soc.* **126**, 15046-15047 (2004).
17. Dommerholt, J., Rutjes, F.P.J.T. & van Delft, F.L. Strain-Promoted 1,3-Dipolar Cycloaddition of Cycloalkynes and Organic Azides. *Top. Curr. Chem.* **374**, 16 (2016).
18. Dehnert, K.W. et al. Imaging the Sialome during Zebrafish Development with Copper-Free Click Chemistry. *ChemBioChem* **13**, 353-357 (2012).
19. Lee, S.B. et al. Mesoporous Silica Nanoparticle Pretargeting for PET Imaging Based on a Rapid Bioorthogonal Reaction in a Living Body. *Angew. Chem., Int. Ed.* **52**, 10549-10552 (2013).
20. Ning, X. et al. Protein Modification by Strain-Promoted Alkyne-Nitrone Cycloaddition. *Angew. Chem. Int. Ed.* **49**, 3065-3068 (2010).
21. Gutmiedl, K., Wirges, C.T., Ehmke, V. & Carell, T. Copper-Free "Click" Modification of DNA via Nitrile Oxide-Norbornene 1,3-Dipolar Cycloaddition. *Org. Lett.* **11**, 2405-2408 (2009).
22. van Berkel, S.S. et al. Metal-Free Triazole Formation as a Tool for Bioconjugation. *ChemBioChem* **8**, 1504-1508 (2007).
23. Song, W., Wang, Y., Qu, J., Madden, M.M. & Lin, Q. A Photoinducible 1,3-Dipolar Cycloaddition Reaction for Rapid, Selective Modification of Tetrazole-Containing Proteins. *Angew. Chem. Int. Ed.* **47**, 2832-2835 (2008).

24. Stöckmann, H., Neves, A.A., Stairs, S., Brindle, K.M. & Leeper, F.J. Exploring isonitrile-based click chemistry for ligation with biomolecules. *Org. Biomol. Chem.* **9**, 7303-7305 (2011).
25. Sletten, E.M. & Bertozzi, C.R. A Bioorthogonal Quadricyclane Ligation. *J. Am. Chem. Soc.* **133**, 17570-17573 (2011).
26. Blackman, M.L., Royzen, M. & Fox, J.M. Tetrazine Ligation: Fast Bioconjugation Based on Inverse-Electron-Demand Diels–Alder Reactivity. *J. Am. Chem. Soc.* **130**, 13518-13519 (2008).
27. Devaraj, N.K., Weissleder, R. & Hilderbrand, S.A. Tetrazine-Based Cycloadditions: Application to Pretargeted Live Cell Imaging. *Bioconjugate Chem.* **19**, 2297-2299 (2008).
28. Mayer, S. & Lang, K. Tetrazines in Inverse-Electron-Demand Diels–Alder Cycloadditions and Their Use in Biology. *Synthesis* **49**, 830-848 (2017).
29. Oliveira, B.L., Guo, Z. & Bernardes, G.J.L. Inverse electron demand Diels–Alder reactions in chemical biology. *Chem. Soc. Rev.* **46**, 4895-4950 (2017).
30. Sauer, J. Diels-Alder reactions II: The Reaction Mechanism. *Angew. Chem. Int. Ed.* **6**, 16-33 (1967).
31. Sauer, J. et al. 1,2,4,5-Tetrazine: Synthesis and Reactivity in [4+2] Cycloadditions. *Eur. J. Org. Chem.* **1998**, 2885-2896 (1998).
32. Devaraj, N.K. & Weissleder, R. Biomedical Applications of Tetrazine Cycloadditions. *Acc. Chem. Res.* **44**, 816-827 (2011).
33. Rossin, R. et al. Highly Reactive trans-Cyclooctene Tags with Improved Stability for Diels–Alder Chemistry in Living Systems. *Bioconjugate Chem.* **24**, 1210-1217 (2013).
34. Clavier, G. & Audebert, P. s-Tetrazines as Building Blocks for New Functional Molecules and Molecular Materials. *Chem. Rev.* **110**, 3299-3314 (2010).
35. Li, Z. & Ding, J. Bisfuran-s-Tetrazine-Based Conjugated Polymers on Synthesis, Characterization, and Photovoltaic Properties. *Macromol. Chem. Phys.* **212**, 2260-2267 (2011).
36. Selvaraj, R. & Fox, J.M. trans-Cyclooctene—a stable, voracious dienophile for bioorthogonal labeling. *Curr. Opin. Chem. Biol.* **17**, 753-760 (2013).
37. Zeglis, B.M. et al. A pretargeted PET imaging strategy based on bioorthogonal Diels–Alder click chemistry. *J. Nucl. Med.* **54**, 1389-1396 (2013).
38. Versteegen, R.M., Rossin, R., ten Hoeve, W., Janssen, H.M. & Robillard, M.S. Click to Release: Instantaneous Doxorubicin Elimination upon Tetrazine Ligation. *Angew. Chem. Int. Ed.* **52**, 14112-14116 (2013).
39. Carlson, J.C.T., Mikula, H. & Weissleder, R. Unraveling Tetrazine-Triggered Bioorthogonal Elimination Enables Chemical Tools for Ultrafast Release and Universal Cleavage. *J. Am. Chem. Soc.* **140**, 3603-3612 (2018).
40. Fan, X. et al. Optimized Tetrazine Derivatives for Rapid Bioorthogonal Decaging in Living Cells. *Angew. Chem. Int. Ed.* **55**, 14046-14050 (2016).
41. Sarris, A.J.C. et al. Fast and pH-Independent Elimination of trans-Cyclooctene by Using Aminoethyl-Functionalized Tetrazines. *Chem. Eur. J.* **24**, 18075-18081 (2018).
42. Versteegen, R.M. et al. Click-to-Release from trans-Cyclooctenes: Mechanistic Insights and Expansion of Scope from Established Carbamate to Remarkable Ether Cleavage. *Angew. Chem. Int. Ed.* **57**, 10494-10499 (2018).
43. Du, S. et al. Cell type-selective imaging and profiling of newly synthesized proteomes by using puromycin analogues. *Chem. Commun.* **53**, 8443-8446 (2017).
44. Rossin, R. et al. Triggered Drug Release from an Antibody–Drug Conjugate Using Fast “Click-to-Release” Chemistry in Mice. *Bioconjugate Chem.* **27**, 1697-1706 (2016).
45. Rossin, R. et al. Chemically triggered drug release from an antibody-drug conjugate leads to potent antitumour activity in mice. *Nat. Commun.* **9**, 1484 (2018).
46. Czuban, M. et al. Bio-Orthogonal Chemistry and Reloadable Biomaterial Enable Local Activation of Antibiotic Prodrugs and Enhance Treatments against *Staphylococcus aureus* Infections. *ACS Cent. Sci.* **4**, 1624-1632 (2018).
47. van Onzen, A. et al. Tetrazine- trans-Cyclooctene Chemistry Applied to Fabricate Self-Assembled Fluorescent and Radioactive Nanoparticles for in Vivo Dual Mode Imaging. *Bioconjug. Chem.* **30**, 547-551 (2019).

48. Li, J., Jia, S. & Chen, P.R. Diels-Alder reaction–triggered bioorthogonal protein decaging in living cells. *Nat. Chem. Biol.* **10**, 1003-1005 (2014).
49. Zhang, G. et al. Bioorthogonal Chemical Activation of Kinases in Living Systems. *ACS Cent. Sci.* **2**, 325-331 (2016).
50. Wilkovitsch, M. et al. A Cleavable C2-Symmetric trans-Cyclooctene Enables Fast and Complete Bioorthogonal Disassembly of Molecular Probes. *J. Am. Chem. Soc.* **142**, 19132-19141 (2020).
51. Keinänen, O. et al. Pretargeted PET Imaging of trans-Cyclooctene-Modified Porous Silicon Nanoparticles. *ACS Omega* **2**, 62-69 (2017).
52. Sullivan, Z. A. et al. T cells regulate the intestinal response to nutrient sensing. *Science* **371**, (2021).
53. Patriarchi, T. et al. An expanded palette of dopamine sensors for multiplex imaging in vivo. *Nat Methods* **17**, 1147-1155 (2020).
54. Costantini, L. M. et al. A palette of fluorescent proteins optimized for diverse cellular environments. *Nat Commun* **6**, 7670 (2015).
55. Rodriguez, E. A. et al. The Growing and Glowing Toolbox of Fluorescent and Photoactive Proteins. *Trends Biochem Sci* **42**, 111-129 (2017).
56. Polonsky, M. et al. Induction of CD4 T cell memory by local cellular collectivity. *Science* **360**, (2018).
57. Arlauckas, S. P. et al. In vivo imaging reveals a tumor-associated macrophage-mediated resistance pathway in anti-PD-1 therapy. *Sci Transl Med* **9**, (2017).
58. Zindel, J. et al. Primordial GATA6 macrophages function as extravascular platelets in sterile injury. *Science* **371**, eabe0595 (2021).
59. Alon, S. et al. Expansion sequencing: Spatially precise in situ transcriptomics in intact biological systems. *Science* **371**, eaax2656 (2021).
60. Cho, C. S. et al. Microscopic examination of spatial transcriptome using Seq-Scope. *Cell* **184**, 3559-3572.e22 (2021).
61. Eng, C. L. et al. Transcriptome-scale super-resolved imaging in tissues by RNA seqFISH. *Nature* **568**, 235-239 (2019).
62. Stickels, R. R. et al. Highly sensitive spatial transcriptomics at near-cellular resolution with Slide-seqV2. *Nat Biotechnol* **39**, 313-319 (2021).
63. Lin, J. R., Fallahi-Sichani, M. & Sorger, P. K. Highly multiplexed imaging of single cells using a high-throughput cyclic immunofluorescence method. *Nat Commun* **6**, 8390 (2015).
64. Pascual-Reguant, A. et al. Multiplexed histology analyses for the phenotypic and spatial characterization of human innate lymphoid cells. *Nat Commun* **12**, 1737 (2021).
65. Radtke, A. J. et al. IBEX: A versatile multiplex optical imaging approach for deep phenotyping and spatial analysis of cells in complex tissues. *Proc Natl Acad Sci U S A* **117**, 33455-33465 (2020).
66. Saka, S. K. et al. Immuno-SABER enables highly multiplexed and amplified protein imaging in tissues. *Nat Biotechnol* **37**, 1080-1090 (2019).
67. Angelo, M. et al. Multiplexed ion beam imaging of human breast tumors. *Nat Med* **20**, 436-442 (2014).
68. Bendall, S. C. et al. Single-cell mass cytometry of differential immune and drug responses across a human hematopoietic continuum. *Science* **332**, 687-696 (2011).
69. Jackson, H. W. et al. The single-cell pathology landscape of breast cancer. *Nature* **578**, 615-620 (2020).
70. Hartmann, F. J. & Bendall, S. C. Immune monitoring using mass cytometry and related high-dimensional imaging approaches. *Nat Rev Rheumatol* **16**, 87-99 (2020).
71. Mahdessian, D. et al. Spatiotemporal dissection of the cell cycle with single-cell proteogenomics. *Nature* **590**, 649-654 (2021).
72. Stoeckius, M. et al. Simultaneous epitope and transcriptome measurement in single cells. *Nat Methods* **14**, 865-868 (2017).
73. McKinnon, K. M. Flow Cytometry: An Overview. *Curr Protoc Immunol* **120**, 5.1.1-5.1.11 (2018).

74. Bechtel, T. J., Reyes-Robles, T., Fadeyi, O. O. & Oslund, R. C. Strategies for monitoring cell-cell interactions. *Nat Chem Biol* **17**, 641-652 (2021).
75. Jenkins, R. W. et al. Ex Vivo Profiling of PD-1 Blockade Using Organotypic Tumor Spheroids. *Cancer Discov* **8**, 196-215 (2018).
76. Voabil, P. et al. An ex vivo tumor fragment platform to dissect response to PD-1 blockade in cancer. *Nature Medicine* 1-12 (2021).
77. Engblom, C. et al. Osteoblasts remotely supply lung tumors with cancer-promoting SiglecF<sup>high</sup> neutrophils. *Science* **358**, (2017).
78. Katzenelenbogen, Y. et al. Coupled scRNA-Seq and Intracellular Protein Activity Reveal an Immunosuppressive Role of TREM2 in Cancer. *Cell* **182**, 872-885 (2020).
79. Pflirschke, C. et al. Tumor-Promoting Ly-6G<sup>+</sup> SiglecF<sup>high</sup> Cells Are Mature and Long-Lived Neutrophils. *Cell Rep* **32**, 108164 (2020).
80. Pucella, J. N., Upadhaya, S. & Reizis, B. The Source and Dynamics of Adult Hematopoiesis: Insights from Lineage Tracing. *Annu Rev Cell Dev Biol* **36**, 529-550 (2020).
81. Armingol, E., Officer, A., Harismendy, O. & Lewis, N. E. Deciphering cell-cell interactions and communication from gene expression. *Nat Rev Genet* **22**, 71-88 (2021).
82. Loughran, S. J., Haas, S., Wilkinson, A. C., Klein, A. M. & Brand, M. Lineage commitment of hematopoietic stem cells and progenitors: insights from recent single cell and lineage tracing technologies. *Exp Hematol* **88**, 1-6 (2020).
83. Ko, J., Oh, J., Ahmed, M. S., Carlson, J. C. T. & Weissleder, R. Ultra-fast Cycling for Multiplexed Cellular Fluorescence Imaging. *Angew Chem Int Ed Engl* **59**, 6839-6846 (2020).
84. Nguyen, S. S. & Prescher, J. A. Developing bioorthogonal probes to span a spectrum of reactivities. *Nat Rev Chem* **4**, 476-489 (2020).
85. Linder, K. E. et al. Synthesis, in vitro evaluation, and in vivo metabolism of fluor/quencher compounds containing IRDye 800CW and Black Hole Quencher-3 (BHQ-3). *Bioconjug Chem* **22**, 1287-1297 (2011).
86. Zaretsky, I. et al. Monitoring the dynamics of primary T cell activation and differentiation using long term live cell imaging in microwell arrays. *Lab on a chip* **12**, 5007-5015 (2012).
87. Wang, G. G. et al. Quantitative production of macrophages or neutrophils ex vivo using conditional Hoxb8. *Nat Methods* **3**, 287-293 (2006).
88. Sykes, D. B. et al. Inhibition of Dihydroorotate Dehydrogenase Overcomes Differentiation Blockade in Acute Myeloid Leukemia. *Cell* **167**, 171-186.e15 (2016).
89. Hidalgo, A., Chilvers, E. R., Summers, C. & Koenderman, L. The Neutrophil Life Cycle. *Trends Immunol* **40**, 584-597 (2019).
90. Gerdes, M. J. et al. Highly multiplexed single-cell analysis of formalin-fixed, paraffin-embedded cancer tissue. *Proc Natl Acad Sci U S A* **110**, 11982-11987 (2013).
91. Schubert, W. et al. Analyzing proteome topology and function by automated multidimensional fluorescence microscopy. *Nat Biotechnol* **24**, 1270-1278 (2006).
92. Oh, J. et al. Rapid serial immunoprofiling of the tumor immune microenvironment by fine needle sampling. *Clin Cancer Res* (2021).
93. de la Torre, D. & Chin, J. W. Reprogramming the genetic code. *Nat Rev Genet* **22**, 169-184 (2021).
94. Lang, K. & Chin, J. W. Cellular incorporation of unnatural amino acids and bioorthogonal labeling of proteins. *Chem Rev* **114**, 4764-4806 (2014).
95. Salic, A. & Mitchison, T. J. A chemical method for fast and sensitive detection of DNA synthesis in vivo. *Proc Natl Acad Sci U S A* **105**, 2415-2420 (2008).
96. Palaniappan, K. K. & Bertozzi, C. R. Chemical Glycoproteomics. *Chem Rev* **116**, 14277-14306 (2016).
97. Cañeque, T., Müller, S. & Rodriguez, R. Visualizing biologically active small molecules in cells using click chemistry. *Nature Reviews Chemistry* **2**, 202-215 (2018).
98. Yang, K. S., Budin, G., Tassa, C., Kister, O. & Weissleder, R. Bioorthogonal approach to identify unsuspected drug targets in live cells. *Angew Chem Int Ed Engl* **52**, 10593-10597 (2013).

99. Nikić, I. et al. Minimal tags for rapid dual-color live-cell labeling and super-resolution microscopy. *Angew Chem Int Ed Engl* **53**, 2245-2249 (2014).
100. Beliu, G. et al. Bioorthogonal labeling with tetrazine-dyes for super-resolution microscopy. *Commun Biol* **2**, 261 (2019).
101. Werther, P. et al. Live-Cell Localization Microscopy with a Fluorogenic and Self-Blinking Tetrazine Probe. *Angew Chem Int Ed Engl* **59**, 804-810 (2020).
102. Wang, J., Wang, X., Fan, X. & Chen, P. R. Unleashing the Power of Bond Cleavage Chemistry in Living Systems. *ACS Cent Sci* **7**, 929-943 (2021).